







ARTICLE

Caldesmon ablation in mice causes umbilical herniation and alters contractility of fetal urinary bladder smooth muscle

Sandra Pütz^{1*}, Lisa Sophie Barthel^{1*}, Marina Frohn^{1*}, Doris Metzler¹, Mohammed Barham², Galyna Prymachuk², Oliver Trunschke¹, Lubomir T. Lubomirov¹, Jürgen Hescheler³, Joseph M. Chalovich⁴, Wolfram F. Neiss², Manuel Koch⁵, Mechthild M. Schroeter¹, and Gabriele Pfitzer¹

The actin-, myosin-, and calmodulin-binding protein caldesmon (CaD) is expressed in two splice isoforms: h-CaD, which is an integral part of the actomyosin domain of smooth muscle cells, and l-CaD, which is widely expressed and is involved in many cellular functions. Despite extensive research for many years, CaD's *in vivo* function has remained elusive. To explore the role of CaD in smooth muscle contraction *in vivo*, we generated a mutant allele that ablates both isoforms. Heterozygous animals were viable and had a normal life span, but homozygous mutants died perinatally, likely because of a persistent umbilical hernia. The herniation was associated with hypoplastic and dysmorphic abdominal wall muscles. We assessed mechanical parameters in isometrically mounted longitudinal strips of E18.5 urinary bladders and in ring preparations from abdominal aorta using wire myography. Ca²⁺ sensitivity was higher and relaxation rate was slower in *Cald1*^{-/-} compared with *Cald1*^{+/+} skinned bladder strips. However, we observed no change in the content and phosphorylation of regulatory proteins of the contractile apparatus and myosin isoforms known to affect these contractile parameters. Intact fibers showed no difference in actin and myosin content, regardless of genotype, although KCl-induced force tended to be lower in homozygous and higher in heterozygous mutants than in WTs. Conversely, in skinned fibers, myosin content and maximal force were significantly lower in *Cald1*^{-/-} than in WTs. In KO abdominal aortas, resting and U46619 elicited force were lower than in WTs. Our results are consistent with the notion that CaD impacts smooth muscle function dually by (1) acting as a molecular brake on contraction and (2) maintaining the structural integrity of the contractile machinery. Most importantly, CaD is essential for resolution of the physiological umbilical hernia and ventral body wall closure.

Introduction

Phosphorylation of the regulatory light chains (RLCs) of myosin at S19 is generally considered to be the major regulatory mechanism that activates smooth muscle contraction (reviewed in Somlyo and Somlyo, 2003; Brozovich et al., 2016). However, force and RLC phosphorylation are frequently uncoupled, e.g., during sustained contractions. This indicates that additional regulatory mechanisms may be present (Morgan and Gangopadhyay, 2001; Pfitzer et al., 2005). The protein caldesmon (CaD) is a candidate for such an actin-associated regulatory mechanism (reviewed in Chalovich et al., 1998; Marston et al., 1998; Gusev, 2001; Wang, 2001).

CaD was initially isolated from chicken gizzard smooth muscle (Sobue et al., 1981) as an integral component of thin filaments (Marston and Lehman, 1985) and was shown to inhibit actomyosin ATPase activity in a Ca²⁺- and calmodulin-dependent manner (Ngai and Walsh, 1984). CaD appears in two major isoform classes, low (l-CaD) and high (h-CaD) molecular weight CaD generated by alternative splicing (Humphrey et al., 1992). While l-CaD is widely expressed in nonmuscle tissues and cells (Mayanagi and Sobue, 2011), h-CaD is found specifically in differentiated smooth muscle (Wang, 2001). Both isoforms share an N-terminal myosin-binding domain (Hemric and Chalovich,

¹Institute of Vegetative Physiology, Center of Physiology, Faculty of Medicine, University of Cologne, Cologne, Germany; ²Institute of Anatomy I, Faculty of Medicine, University of Cologne, Cologne, Germany; ³Institute of Neurophysiology, Center of Physiology, Faculty of Medicine, University of Cologne, Cologne, Germany; ⁴Department of Biochemistry & Molecular Biology, Brody School of Medicine at East Carolina University, Greenville, NC; ⁵Institute for Dental Research and Oral Musculoskeletal Biology, Faculty of Medicine and University Hospital Cologne, University of Cologne, Cologne, Germany.

*S. Pütz, L.S. Barthel, and M. Frohn contributed equally to this study; Correspondence to Gabriele Pfitzer: gabriele.pfitzer@uni-koeln.de; Mechthild M. Schroeter: mechthild.schroeter@uni-koeln.de; L.T. Lubomirov's present address is Institute of Physiology, Brandenburg Medical School Theodor Fontane, Brandenburg an der Havel, Germany.

This work is part of a special collection on myofilament function and disease.

© 2021 Pütz et al. This article is distributed under the terms of an Attribution–Noncommercial–Share Alike–No Mirror Sites license for the first six months after the publication date (see <http://www.rupress.org/terms/>). After six months it is available under a Creative Commons License (Attribution–Noncommercial–Share Alike 4.0 International license, as described at <https://creativecommons.org/licenses/by-nc-sa/4.0/>).

1988; Ikebe and Reardon, 1988) and a C-terminal actin-binding domain (Szpacenko and Dabrowska, 1986). The latter also provides binding sites for tropomyosin (TM), calmodulin, and cortactin (Gusev, 2001) and is responsible for inhibition of actin-activated myosin ATPase activity with proteins in solution (Szpacenko and Dabrowska, 1986; Velaz et al., 1990; Marston et al., 1998) and for inhibition of contraction in skinned fibers (Pfitzer et al., 1993). Inhibition is enhanced by TM (Horiuchi and Chacko, 1989; Chalovich et al., 1998). Binding of Ca^{2+} -calmodulin or phosphorylation of CaD by a number of protein kinases reverses this inhibition (Wang, 2001). CaD may also facilitate contraction by stabilizing actin (Wang, 2001; Mayanagi and Sobue, 2011) and myosin (Katayama et al., 1995) filaments and by tethering actin and myosin filaments together (Hemric and Chalovich, 1988; Marston et al., 1992). The subcellular localization of h-CaD in the actin-myosin domain of smooth muscle cells (Fürst et al., 1986) is consistent with the proposed function of h-CaD as a regulator of smooth muscle contraction as outlined below. In nonmuscle cells, l-CaD is involved in stress fiber and microfilament reorganization and is localized to membrane ruffles and lamellipodial extensions in migrating cells (Lin et al., 2009; Jiang et al., 2010; Mayanagi and Sobue, 2011). l-CaD may participate in diverse cellular functions such as cytokinesis (Yamashiro et al., 1994), podosome formation (Gu et al., 2007), and hormone release (Janovick et al., 1991; Castellino et al., 1992).

Much of the evidence suggests that the primary function of CaD in smooth muscle cells is to act as a molecular brake on contraction. Lowering CaD levels increased Ca^{2+} sensitivity (Malmqvist et al., 1996) and enabled cross-bridge cycling under resting conditions (Earley et al., 1998). Interfering with CaD binding to actin increased force under resting conditions (Katsuyama et al., 1992), while loading of skinned fibers with exogenous CaD inhibited force at constant RLC phosphorylation (Pfitzer et al., 1993) and increased the rate of relaxation (Albrecht et al., 1997). Incubation of Triton X-100-skinned fibers with p21-activated kinase (Pak) increased phosphorylation of CaD and elicited a contraction without an increase in RLC phosphorylation (Van Eyk et al., 1998).

The *in vivo* importance of these findings was suggested by increased expression of CaD in the pregnant uterus and inhibition of CaD via phosphorylation during delivery (Li et al., 2009). Down-regulation of CaD in zebrafish larvae with morpholinos suggested that CaD plays a crucial role in vasculo- and angiogenesis (Zheng et al., 2008), morphogenesis of the heart, and intestinal peristalsis (Abrams et al., 2012). Germline deletion of h-CaD in mice resulted in a high occurrence of umbilical hernia and perinatal death (Guo et al., 2013). Aortas from surviving adults exhibited a slowed relaxation and a lower active force. In visceral smooth muscles, l-CaD expression was up-regulated, which may compensate for the loss of h-CaD (Guo et al., 2013). In another mouse model, the introduction of five point mutations within the C terminus of CaD, which encompassed the ATPase inhibitory determinants, resulted in a lethal phenotype in homozygous but not heterozygous (HET) mice (Deng et al., 2013). Adult HET mice displayed nonvoiding contractions during urinary bladder filling. Force production in response to KCl and electrical field stimulation was increased.

To further probe the *in vivo* role of CaD, we ablated 38 kb of the murine *Cald1* gene, thereby preventing expression of both isoforms of CaD. HET mice displayed no overt phenotype; however, homozygous offspring were not viable, most likely due to umbilical herniation of the intestines present in term fetuses, indicating that CaD is essential for resolution of the physiological umbilical hernia, which is typically completed at embryonic day 16.5 (E16.5). We observed no further major macroscopic malformations. To explore the effect of CaD depletion on smooth muscle contractile properties, we chose urinary bladders from near-term fetuses, because bladder smooth muscle, in contrast to aorta and intestinal smooth muscle, matures before birth and responds to stimulation with contractile agonists (Arens et al., 2000). The authors propose that this reflects the fact that the bladder is functional early in midterm pregnancies and excretes urine, which is related to the production of amniotic fluid. Our results on contractile function are compatible with a dual function of CaD: (1) it acts as a brake on smooth muscle contraction, and (2) it is involved in maintaining the structural integrity of the contractile apparatus.

Materials and methods

Animals

The generation of the B6-*Cald1* knockout (KO) mouse line and the current study were approved by Landesamt für Natur, Umwelt und Verbraucherschutz NRW (permit numbers AZ 8.87-50.10.31.08.235 and AZ 84-0.02.2015.A054) and supervised by the Institutional Animal Care and Use Committee. The experiments were performed in accordance with the guidelines of the European Commission (Directive 2010/63/EU) and the German animal welfare act (TierSchG). All mice were bred and kept in temperature-controlled, enriched cages with 12-h light/dark cycles in the animal facility of the Medical Faculty of the University of Cologne. Mice had free access to water and chow (ssniff). The dams were humanely sacrificed between E14.5 \pm 0.5 and E19.5 \pm 0.5 (timed breeding, determined with plaque test), and the fetuses were euthanized as approved. In this study, littermates of both sexes from HET timed breeding pairs were used. In the majority of experiments, *Cald1*^{+/+} littermates, denoted WT, served as controls. Because of limited numbers of *Cald1*^{+/+} fetuses, we used WT mice of the same genetic background (C57BL/6N) bred in the same facility and under the same conditions as the B6-*Cald1* KO mouse line in a few experiments as controls. This report followed the Animal Research: Reporting of *In Vivo* Experiments (ARRIVE) guidelines for reporting animal experiments.

Gene targeting

Cald1^{+/-} mice and *Cald1*^{-/-} embryos were generated on the C57BL/6J background using standard techniques (Fig. 1). Briefly, a 200-bp fragment 1.69 kb upstream of exon 2 was amplified by PCR introducing, beside the flanking XhoI-EcoRI restriction sites, an additional internal 5' EcoRV site. After sequencing, the fragment was cloned into the PL451 vector using the flanking XhoI and EcoRI restriction sites. For the 3'-arm, a 208-bp fragment was generated by PCR, located 1.08 kb downstream of the

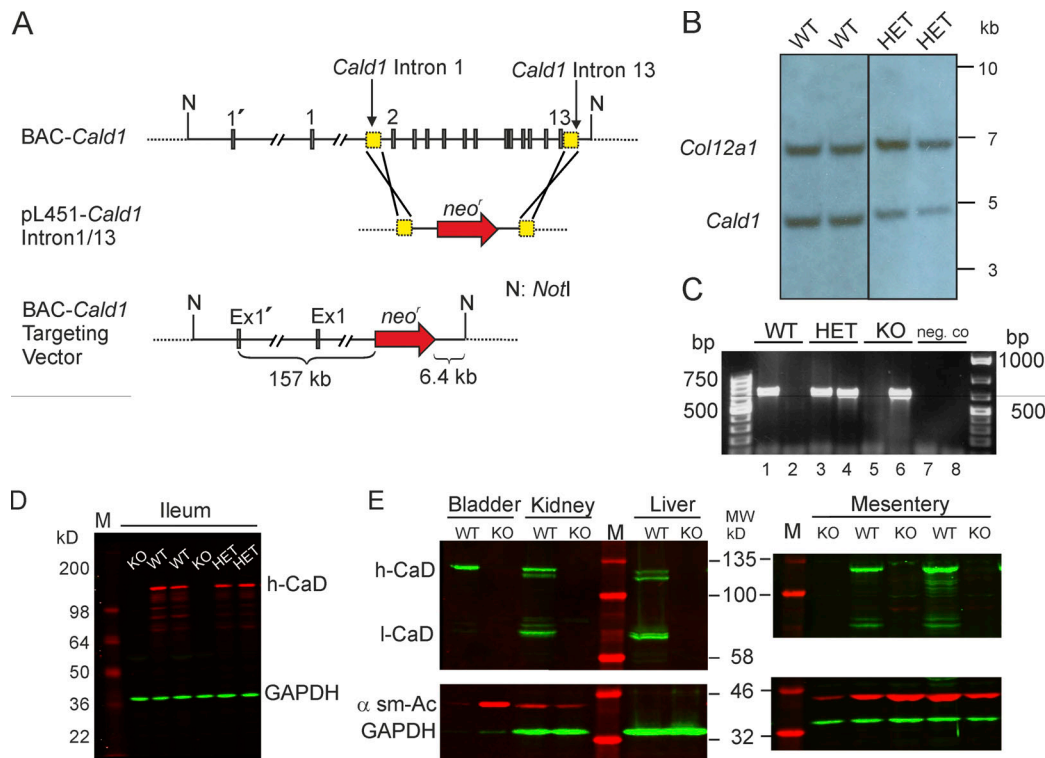


Figure 1. Targeting the *Cald1* gene. (A) Using clone RPC123–104H13 as *Cald1* gene template, the *Cald1* BAC targeting construct was generated by bacterial engineering, linearized with *NotI*, and electroporated into V6.5 ES cells. (B) DNA of G418 selected ES cell clones were isolated, digested by the endonuclease *Bam*HI, and analyzed by semiquantitative Southern blot using a probe against *Col12a1* for signal standardization. The internal *Cald1* probe showed signal intensity reduced by half in ES cell clones with homologous recombination events. (C) Genotype of the offspring from mating *Cald1*^{+/-} × *Cald1*^{+/-} was determined in two separate PCR reactions. The primers for the WT band were located within the ablated *Cald1* sequence (lanes 1, 3, and 5); one of the primers for detection of the homologous recombination event was located within the neomycin selection cassette, and the other in the *Cald1* gene (lanes 2, 4, and 6). (D and E) Representative Western blots from lysates from E18.5 ileal smooth muscle (D), urinary bladder, kidney, liver, and mesentery (E) using antibodies against CaD and GAPDH (loading control) and smooth muscle α-actin (α-smAct). In liver, kidney, and mesentery artery, CaD is less abundant than in bladder. To get a signal intensity from these tissues comparable to that of bladder, 40 times more protein had to be loaded. No CaD signal was detected in KO (*Cald1*^{-/-}) tissue; signal intensity was reduced in HET ileum (*Cald1*^{+/-}) compared with WT littermates (*Cald1*^{+/+}). Expression of GAPDH was not affected by the mutation.

Cald1 stop codon. For facilitated ligation into the PL451 vector, flanking *Bam*HI and *Sac*II restriction sites were introduced. An additional internal 3' *Eco*RV restriction site was generated to allow excision of the fragment. After confirming the sequence, the *Bam*HI and *Sac*II sites were used for subcloning into the PL451 vector, which already contained the 5' *Cald1* sequence. The genomic fragment, containing the PGKneo cassette, was released by digestion with *Eco*RV and used for BAC recombineering to generate the BAC *Cald1* targeting vector. The RPC123-104H13 clone, containing the *Cald1* locus, was transformed into EL250, with the released *Eco*RV-*Eco*RV fragment mentioned above, and activated for recombination (Liu et al., 2003). The resulting BAC targeting vector was subjected to PCR and restriction analysis to confirm the correct integration of the *Eco*RV-flanked fragment. Subsequently, the targeting vector was transformed into DH10B *Escherichia coli*, purified with a Qiagen Endo-free Plasmid Purification kit, linearized with *NotI*, and used for targeting the genomic *Cald1* locus in V6.5 ES cells (gift from Rudolf Jaenisch, Whitehead Institute, Cambridge, MA). The latter was performed by Biocenter Oulu, Oulu, Finland. DNA of clones with G418 resistance was analyzed by semiquantitative Southern blotting. For this, the genomic DNA was digested with *Bam*HI, subjected to gel

electrophoresis, transferred to Hybond N⁺ membrane, and simultaneously hybridized with *Cald1* (518 bp) and a *COL12A* probe (623 bp). The latter was used for quantification of the signals. In cases where homologous recombination had taken place, the *Cald1* signal (4.9 kb) was reduced by 50% in comparison to the *COL12A1* control signal (6.87 kb; Fig. 1 B). Of ~150 clones, 3 clones had undergone homologous recombination at the *Cald1* gene locus. One clone was injected into C57BL/6 blastocysts. Male offspring presenting a high level of chimerism were backcrossed to C57BL/6N mice for >10 generations. Genotyping of the back breeding was performed by PCR (Fig. 1 C). The primers are listed in Table 1.

Light microscopy

Immediately after sacrificing the dams, the fetuses were procured and fixed for 1 h in 4% paraformaldehyde (PF), followed by removal of the skin. Thereafter, they were fixed in 4% PF at 4°C overnight, dehydrated with an ascending ethanol series, embedded in paraffin, and sectioned at 7.5 μm in the sagittal direction. Every other fifth section was stained with either Nissl stain or Trichrome (Masson-Goldner). Sections were imaged with a Leica SCN400 light microscope. The spines of the fetuses

Table 1. Primers for amplification of 5'- and 3'-arm and for screening

Primer	Sequence ^a	Location
Cloning		
5'-arm forward	AACTCGAGGATATCAAGATGATGGTCCCATAC	34739922–34739944 ^b
5'-arm reverse	GAGAATTCTCCATAAATATGACAGGAAGAGTAG	34740097–34740121 ^b
3'-arm forward	AAGGATCCCTTCTCTACCACTTAGAACCAAG	34774307–34774329 ^b
3'-arm reverse	ATCATACCGCGGATATCAACTTATGACCGTACCAACTG	34774490–34774510 ^b
Southern		
Cald1 forward	<u>CTACCACAAACCTTACTGCTGAGC</u>	69123–69100 ^c
Cald1 reverse	<u>GGTGCTGGCCTCATTGAAA</u>	68582–68601 ^c
COL12A1 forward	<u>GATGGTACTTACAGATATATGG</u>	Collagen, type XII α 1 126865–126844 ^c
COL12A1 reverse	<u>GCAAAGAGGAGCAGGAAAAGG</u>	Collagen, type XII α 1 126242–126262 ^c
Genotyping		
Cald1 forward	<u>CATCAAGTCCTACCAGAAGAA</u>	80083–80063 ^d
Cald1 reverse	<u>CCCTTTCATTCACTCCTTTCC</u>	79392–79412 ^d
neomycin	CATCGCATTGTCTGAGTAGG	Neomycin
Cald1 reverse	<u>TTTGTAATGACGCTGTATGC</u>	51269–51290 ^d

^aGene-specific sequence is underlined.

^bCaD 1, GeneID accession number 109624; chromosome 6, NC_000072.6.

^c*Mus musculus* BAC clone RP24-141A7 from chromosome 9, GenBank accession number AC157477.2.

^d*Mus musculus* 6 BAC RP23-104H13, complete sequence.

were used for orientation to ensure that measurements were at comparable planes. Special care was taken to ensure that the spine with the spinal cord in the center was completely reflected. Starting from the center slide, the next section on either side was used for determination of the areas of the different urinary bladder layers at 10-fold magnification. The values from these three determinations were averaged; the mean was taken for further statistical analysis. The different tissue layers (urothel, lamina propria, tunica muscularis, and lumen) were color marked with the program GIMP (v2.10.12). The number of pixels (px) per marked area was calculated with a Python script, and the area in square millimeters was estimated with a conversion factor of 518,400 px/mm².

For histological analysis of the abdominal wall, skin flaps (~12 mm in transversal and 5–6 mm in rostral-to-caudal direction), covering the umbilicus or the omphalocele, respectively, were dissected together with the muscles that lie underneath from E17.5 *Cald1*^{+/+}, *Cald1*^{+/-}, and *Cald1*^{-/-} fetuses. The mesenteries from these animals were used for other investigations (3R principle). The skin flaps were mounted flat at their in situ length on Sylgard-coated dishes, fixed with 4% PF in PBS for 7 d at 4°C, and embedded as described above. Transverse sections (5 μ m) were obtained using a rotary microtome (Microm HM 340E; Thermo Fisher Scientific). After deparaffinization and rehydration, the sections were stained at room temperature with hematoxylin and eosin according to standard procedures and imaged with a Zeiss AX10 light microscope using a Hitachi HV-F202 camera.

Electron microscopy (EM)

EM methods are discussed in the Supplemental text at the end of the PDF.

Wound healing assays

WT and CaD-deficient E14.5 \pm 0.5 embryonic fibroblasts were seeded in equal concentrations of $2 \times 10^5/3$ ml onto 35-mm CellBind culture dishes (Corning) using Dulbecco's modified Eagle Medium (DMEM)-complete (DMEM high glucose, 10% FBS, 2 mM L-glutamine, 100 units/ml penicillin-streptomycin, and 1 \times nonessential amino acids). After ~48 h, the cells were confluent, so the medium was removed completely, and cell wounds were made in the monolayer using a premium surface 200- μ l pipet tip (Nerbe Plus). Cells were rinsed twice with DMEM, 3 ml each, and overlaid with 3 ml DMEM-complete medium. Wound closure was documented by JuLi Br Live cell movie analyzer (Peqlab) over a time frame of 24 h, using a P4x plus digital zoom objective and a high-resolution digital camera containing a 5-megapixel CMOS-color sensor, resulting in images of 2,560 \times 1,920 px. For analysis with ImageJ software, 25 images were acquired on an hourly basis, and the distance between the cell boundaries was determined (in pixels) at four previously set positions.

Tissue preparation for biochemical and mechanical experiments

Immediately after sacrificing the animals, the organs were removed, weighed, shock frozen, and stored at –80°C for biochemical

analysis. Alternatively, the urinary bladders and aortae were prepared for mechanical experiments. It was technically not possible to remove the urothel from the tunica muscularis in fetal bladders; thus, protein content and mechanical output reflect that of the bladder wall.

Actin and myosin content

Fetal urinary bladders were pulverized under liquid nitrogen and extracted in 60 μ l/mg sample buffer wet weight. The sample buffer contained 4 mM urea, 50 mM Tris/HCl, pH 6.8, 1% SDS, 10 mM dithiothreitol (DTT), and a protease inhibitor cocktail, cOmplete (Roche). Actin and myosin contents were quantified in lysates from E18.5 urinary bladders from *Cald1*^{-/-} and *Cald1*^{+/-} littermates using myosin and actin standard curves, and protein isolation as described (Schroeter and Chalovich, 2005). Densitometric scans of Coomassie Brilliant Blue-stained gels were evaluated with Phoretix 1D advanced software v5.0.

Western blot analysis

Lysates from organs and mesenteries were obtained by homogenization of the tissues in 30 μ l urea-free sample buffer (30 μ l/mg tissue) in glass microhomogenizers, followed by boiling at 95°C for 5 min. Urea was added once the homogenates were cooled down to room temperature. Tissues were extracted for 1 h on ice and centrifuged at 14,000 rpm for 10 min. Proteins of the supernatants were separated by SDS-PAGE. Proteins were transferred to nitrocellulose membranes (pore size 0.1 μ m; Protran; Amersham) in 25 mM Tris, 192 mM glycine (transfer buffer), 20% methanol, and 0.05% SDS for 20 h at 27 V and 4°C. Transfer was visualized with Ponceau red, and nonspecific binding sites of the membranes were blocked with Tris-buffered saline (TBS; 10 mM Tris and 150 mM NaCl) containing 0.5% fat-free dry milk (Applichem; TBS-milk). The blots were incubated overnight at 4°C with the primary antibodies in TBS-milk, which with some antibodies contained Tween (TBST, concentrations of Tween given with the respective antibody) according to the manufacturer's recommendations. Primary antibodies: affinity purified anti-CaD (1:1,000, 0.1% Tween, custom-made in rabbits against recombinant murine h-CaD by Pineda Antikörper-Service, Berlin), anti-MLCK (1:10,000, 0.05% Tween, #M7905; Sigma-Aldrich), anti-PKC α (1:20,000, 0.05% Tween, #P4334; Sigma-Aldrich), anti-fascin (1:1,000, 0.1% Tween, #54545S; Cell Signaling), anti-calponin (1:5,000, 0.1% Tween, kind gift from Prof. Dr. U. Gröschel-Stewart, Technical University of Darmstadt, Darmstadt, Germany), anti-PP1 δ (1:500, #07-270; Upstate Biotechnology), SM22 (1:20,000, 0.1% Tween, #NB600-507; Novus Biologicals), and anti-nonmuscle myosin heavy chain IIA (1:1,000, 0.1% Tween, #M8064, lot 038M4800V; Sigma-Aldrich). After washing the membranes three times for 5 min with TBST, the blots were incubated with the appropriate secondary antibodies (H+L, DyLight 680, and DyLight 800 [1:10,000; Thermo Fisher Scientific]) in TBST for 1 h at room temperature, followed by washing the membranes three times for 5 min in TBST and one time for 5 min in TBS. Immunoreactivity was visualized and quantified with the Li-Cor Odyssey infrared imager.

MYPT1 phosphorylation

Lysates from shock-frozen urinary bladders were prepared in lysis buffer containing (in mM): 20 Tris-HCl, pH 7.4, 2 orthovanadate, 2 molybdate, 2 Na-pyrophosphate, 2 benzamidine, 0.5 aprotinin, 1 PMSF, 2% Triton X-100, 0.4% SDS, and 0.1% bromophenol blue. Proteins were separated by 4–20% gradient SDS-PAGE and transferred to nitrocellulose with 0.005% SDS containing transfer buffer. The membranes were blocked with 2% milk for 1 h and probed with primary antibodies overnight: anti-phospho-T696-MYPT1 (1:40,000, 0.1% Tween, #ABS45, Lot 2181279; Millipore), anti-phospho-T853-MYPT1 (1:2,000, #36-003, lot 2032258; Millipore), anti-MYPT1 (1:5,000, 0.05% Tween, #612165, lot 7138563; BD), for loading control anti-GAPDH (1:40,000, #G9545, Lot 127M4814V; Sigma-Aldrich), and anti-SM22 (1:20,000, 0.1% Tween, #NB600-507, lot C2E090713; Novus Biologicals). After washing the blots, they were incubated with appropriate secondary antibodies for 1 h at room temperature. Immunoreactive signals were quantified as above.

Mechanical experiments in chemically skinned longitudinal bladder strips

After weighing, the whole bladders were chemically permeabilized with 1% Triton X-100 for 60 min on ice as in Wirth et al. (2003). The skinned preparations were stored in relaxing solution (see below) containing 50% vol/vol glycerol at -20°C until use. For force measurements, we cut the bladders in half in the longitudinal direction (base to apex). Thus, two strips per bladder were obtained, but we used only one in a given experimental protocol unless stated otherwise. The strips were mounted horizontally between a KG7S or KG3 force transducer (Scientific Instruments) and a fixed post in an organ bath at room temperature containing relaxing solution. The distance between the force transducer and the post could be adjusted by a micrometer drive. The initial length, L_0 , was determined by slackening and restretching the preparations until force was just discernable. In initial experiments, the optimal length was assessed to be $1.5L_0$ from force-length relationships. Following an initial maximal contraction/relaxation cycle at $1.5L_0$, the strips were incubated in solutions with cumulatively increasing $[Ca^{2+}]$ to obtain force-pCa relationships ($pCa = -\log[Ca^{2+}]$). At the end of the experiments, the preparations were weighed, and the cross-sectional area was determined as (wet weight in mg / length at L_0 in mm \times 1 mg/mm³) (cf. Murphy et al., 1974). All experiments were performed at room temperature. Relaxing solution consisted of (in mM): 20 imidazole, 7.5 ATP, 10 Mg-acetate, 10 creatine phosphate, 4 EGTA, 1 NaN₃, 5 DTT, 1 μ M leupeptin, 0.5 μ M calmodulin, and 140 U/ml creatine kinase, pH 6.7 at 22°C. Contraction solution contained, in addition, 4 mM CaCl₂. Intermediate $[Ca^{2+}]$ was obtained by mixing relaxation and contraction solution in the appropriate ratio, and free $[Ca^{2+}]$ was calculated as in Wirth et al. (2003).

RLC phosphorylation in permeabilized bladder strips

RLC phosphorylation was determined with 2-D-PAGE. Isometrically mounted strips were fixed at the desired time point in 10% trichloroacetic acid (TCA) in acetone precooled to 4°C and

stored at -80°C overnight. The next day, the strips were washed with acetone, dried, and stored at -80°C until further processing. The strips were homogenized and extracted for 2 h at room temperature in urea buffer containing 9.2 M urea, 0.1 M Tris-HCl, pH 7.5, 20 $\mu\text{l}/\text{ml}$ ampholines, pH 4.5–5.4, 60 mM DTT, and 0.01% bromophenol blue. Proteins were separated by isoelectric focusing in the first dimension in a solution containing 3.3% acrylamide/bisacrylamide (28:1.6), 0.8% Triton X-100, 4.3% ampholines, pH 4.5–5.4, and 1.33% ampholines pH 3–10, ammonium persulfate (0.07%), and tetramethylethylenediamine (0.06%). Proteins were separated at 600 V for 4 h in the first dimension, followed by 12.5% SDS-PAGE in the second dimension. Proteins were visualized with silver staining and analyzed using the Phoretix System. In some experiments, the 12.5% SDS-PAGE (29:1 acrylamide/bisacrylamide) contained 5 mM Phos-Tag and 80 μM MnCl_2 according to Moreno-Domínguez et al. (2013). Proteins were transferred to nitrocellulose and probed with antibodies directed against RLC (MRLC3 1:1,000, #SC-15370; Santa Cruz) and phosphospecific antibodies directed against pS19-RLC (1:1,000, #600-401-416; Rockland). Immunoreactivity was visualized and evaluated as above.

Mechanical experiments in E18.5 intact longitudinal bladder strips

Fetal urinary bladders were split in half and mounted in the myograph in physiological salt solution (PSS) containing (in mM): 118 NaCl, 5 KCl, 1.2 Na_2HPO_4 , 24 HEPES, 1.2 MgCl_2 , 0.16 CaCl_2 , and 10 glucose, pH 7.4, and continuously gassed with 100% O_2 . After determining L_0 as described above, CaCl_2 was increased to 1.6 mM and temperature was raised to 37°C . The strips were allowed to equilibrate for ≥ 30 min before resting, and active length–tension curves were obtained. At each length, they were stimulated twice with 80 mM KCl (equimolar replacement of NaCl). Finally, the strips were stimulated with increasing concentrations of carbachol. At the end of the experiments, the tissues were weighed, and cross-sectional area was determined as above.

Wire myography with intact ring preparations from E18.5 aorta

Immediately after isolation of the urinary bladder, the aorta was removed from the fetuses and placed in HEPES-buffered, low- Ca^{2+} PSS solution (0.16 mM CaCl_2 , see below) for 10 min. Thereafter, ring preparations of the abdominal aorta between the branching of the renal arteries and the bifurcation of the iliac arteries were obtained and mounted in a wire myograph (model 610A; Danish Myotechnology) on 25- μm -diameter tungsten wires in low- Ca^{2+} PSS as in Lubomirov et al. (2017). 10 min after mounting, the low- Ca^{2+} PSS solution containing (in mM) 119 NaCl, 4.7 KCl, 1.17 KH_2PO_4 , 1.17 MgSO_4 , 0.16 CaCl_2 , 5.5 glucose, 25 NaHCO_3 , and 0.03 EGTA, pH 7.4, was replaced with carbogen (95% O_2 /5% CO_2)-aerated PSS containing 1.6 mM CaCl_2 , and the temperature was raised to 37°C . The preparations were pre-stretched according to the Mulvany normalization protocol (Mulvany and Halpern, 1977) as given by the manufacturer (Danish Myotechnology) as in Lubomirov et al. (2017) but only up to a calculated transmural pressure of 6 kPa (50 mmHg)

because of the lower fetal blood pressure. This was followed by releasing the preparations to IC_{90} , i.e., 90% of the internal circumference at 6 kPa (aortas from three KO and three WT fetuses). Alternatively, they were stretched directly to a passive force of ~ 1 mN (aortas from two WT and four KO fetuses). As the prestretching steps were similar, we did not analyze subgroups. Following an equilibration period (30 min), the aortas were incubated with cumulatively increasing concentrations of the thromboxane analogue U46619. Following relaxation, a second dose–response relation was obtained in the presence of *N*-nitroarginine methyl ester (L-NAME; $n = 3$ per group). The pH was kept at 7.4 with carbogen throughout the experiment. All substances were added directly to the organ bath.

Data evaluation and statistical analysis

Mechanical data were recorded with LabChart 7 (AD Instruments) at a sampling rate of 40 Hz. The data were analyzed with Excel and GraphPad Prism v8.0. We present all results as mean \pm SD, with n reporting the number of fetuses unless stated otherwise. The force–pCa and dose–response relations were fitted with a sigmoidal function provided by GraphPad Prism. In some experiments, force measurements in skinned fibers were performed on both strips from a given bladder. In this case, the results from the two experiments were averaged; the mean was taken for further statistical analysis. Normal distribution was tested with Shapiro–Wilk normality test. Significance was tested with unpaired Student's *t* test when two sets of data were compared, with one-way ANOVA for multiple comparisons within one group, and two-way ANOVA for multiple comparisons between groups; if significant, Sidak's multiple comparisons posttest or Kruskal–Wallis test followed by Dunn's multiple comparisons test were used as appropriate. The significance level was set at $P < 0.05$; exact *P* values are given for $0.01 > P > 0.1$.

Online supplemental material

Fig. S1 shows hematoxylin and eosin–stained sections of the abdominal wall from E17.5 fetuses at a larger magnification than in Fig. 4 and images of a second KO and one HET animal. Fig. S2 shows electron micrographs from E18.5 bladder smooth muscle. Supplemental text at the bottom of the PDF describes EM methods relevant for Fig. S2.

Results

Litter characteristics and pathological anatomy of *Cald1*^{−/−} offspring

Our targeting vector spanned the *Cald1* gene from intron 1 to intron 13 (Fig. 1 A). Homologous recombination with this vector restricted CaD protein synthesis to the first 20 or 24 amino acids at the N terminus, thus ablating all functional relevant domains of both isoforms. Western blots with affinity-purified rabbit antibodies raised against mouse CaD confirmed the absence of h-CaD in smooth muscles (ileum and urinary bladder; Fig. 1, D and E) and of both isoforms in kidney, liver, and the mesentery (Fig. 1 E) from *Cald1*^{−/−} fetuses. The mesentery from *Cald1*^{+/+} fetuses expressed predominantly h-CaD, as it is rich in blood vessels.

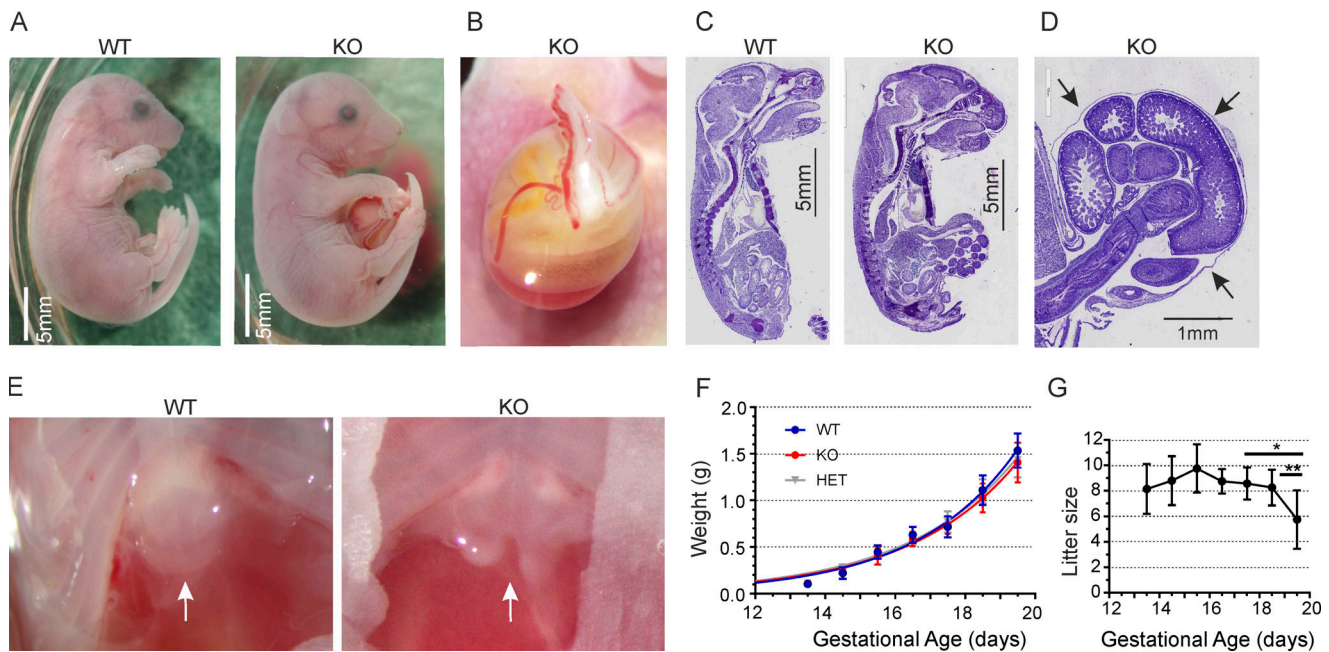


Figure 2. Phenotype of WT and *Cald1*^{-/-} E18.5 animals. (A) In contrast to WT (*Cald1*^{+/+}), *Cald1*^{-/-} littermates (KO) displayed an umbilical hernia; white bars, 5 mm. (B) Enlarged view of the umbilical hernia. (C) Nissl stain of sections of E18.5 fetuses. (D) Enlarged view showing that the umbilical hernia is covered with membranes (arrows) characteristic of an omphalocele. (E) Impaired fusion of the lower sternum (xiphoid, arrows) in KO as opposed to WT. (F) Relation between body weight and gestational age; symbols represent mean \pm SD; $n = 3$ –70 fetuses; solid lines: monoexponential fit (rate constants; $k_{WT} = 0.345$ d, $k_{KO} = 0.321$ d, k is not different between datasets). (G) Relation between litter size and gestational age. The litter size was not different between E13.5 and E18.5 litters but was lower in E19.5 litters; symbols represent mean \pm SD; the number of litters at each gestational age is given in Table 2. *, $P < 0.05$; **, $P < 0.01$ (one-way ANOVA followed by Sidak's multiple comparison test).

No homozygous *Cald1*^{-/-} offspring were obtained. The most likely cause of lethality was the persistence of the physiological umbilical hernia until term (Fig. 2, A–D; and Table 2). If present at birth, an umbilical hernia triggers maternal cannibalism. The physiological umbilical hernia contains the growing midgut within a mesenchymal sac. The gut relocates to the abdominal cavity, and by E16.5, the ventral abdominal wall has completely closed around the umbilical vessels (Brewer and Williams, 2004). In line with this, only 1.5% (2/136) of E17.5–E19.5 *Cald1*^{+/+} fetuses presented with an umbilical hernia. In contrast, an umbilical hernia persisted in \sim 97% *Cald1*^{-/-} and \sim 10% *Cald1*^{+/-} of E17.5–E19.5 fetuses (compare Table 2). The herniation was covered by a membrane, pathognomonic of an omphalocele as opposed to a gastroschisis (Fig. 2, B and D; Carnaghan et al., 2013). In addition, the xiphoid was incompletely fused with near 100% penetrance (Fig. 2 E). In approximately one third of the fetuses, parts of the liver were herniated in addition to the gut (so-called giant hernia). In \sim 85% of KO fetuses, the liver exhibited whitish spots. The trias omphalocele, split xiphoid, and whitish liver spots predicted homozygosity at close to 100%. Otherwise, no further macroscopic or gross microscopic anomalies of the organs were detected (Fig. 2 C), but we cannot exclude pathologies of the microarchitecture. Nissl-stained sections of the fetuses suggested a subtle loss of order of the matrix (Grundsubstanz) between the visceral organs (Fig. 2 C). *Cald1*^{-/-} offspring without an omphalocele displayed no overt anomalies. They were viable, fertile, and reached old age.

Neither Mendelian nor sex distribution was markedly violated between E13.5 and E18.5 (Table 2). The growth curves of the genotypes were similar between E14.5 and E17.5, but late in pregnancy (E18.5), the body weight was \sim 10% ($P = 0.03$) lower in KO than in WT (Fig. 2 F). The average litter size in HET pairing at E18.5 was 8.5 ± 1.5 fetuses per litter ($n = 48$ litters) and did not differ between E13.5 and E17.5 (Fig. 2 G and Table 2). At E19.5, it was significantly lower compared with E17.5 and E18.5 litters (6 ± 2 fetuses per litter, $n = 12$ litters). Occasionally we found resorbed fetuses, which may account for the decline in litter size at E19.5. For animal welfare reasons, it was not possible to compare these numbers to WT breeding. However, the number of WT neonates per litter of the same genetic background (C57BL/6N), which were bred and kept under the same conditions as the B6-*Cald1* KO mouse line, was 6.4 ± 2.7 ($n = 25$ litters). Thus, there appeared to be no major deviation from normal litter size.

CaD might be involved in implantation of the embryo (Kilpatrick et al., 2009; Paule et al., 2010). In line with this, it seemed that HET mating resulted in fewer pregnancies than WT breeding. However, we did not quantify this. Given the presumed function of CaD for silencing of uterine contractions during pregnancy (Li et al., 2009), we hypothesized that the genotype of the dam in WT \times HET mating would matter. However, we found no difference in litter size between WT \times HET and HET \times WT pairing ($P > 0.05$). To avoid premature birth, pregnancies were terminated at the latest by E19.5, and most

Table 2. Litter size, Mendelian and sex distribution, and prevalence of omphalocele

Variable	E13.5	E14.5	E15.5	E16.5	E17.5	E18.5	E19.5
Litters							
Animals per litter	8 ± 2	9 ± 2	10 ± 2	9 ± 1	8 ± 1	8 ± 2	6 ± 2
Number of litters	7	5	4	8	10	48	12
Mendelian distribution							
WT/KO/HET	15/11/26	11/13/24	11/11/14	14/15/40	26/11/43	95/94/205	15/10/40
Total number of fetuses	57	44	39 ^a	69	81 ^b	401 ^c	68
Sex distribution (M/F)^d							
WT	21/9	16/9	12/18	17/11	13/16	17/9	5/18
KO	10/10	11/18	14/14	10/10	12/0	12/8	0/14
HE	37/12	34/12	15/25	31/20	26/31	17/20	37/18
Omphalocele^e							
WT					2/26 (8%)	0/95 (0%)	0/15 (0%)
KO					11/11 (100%)	86/94 (92%)	10/10 (100%)
HET					3/45 (7%)	15/205 (7%)	6/40 (15%)

Data are mean ± SD, n, or n/total n in group (%). At E18.5, total number of animals is higher than for litter size, as it combines numbers from two cohorts.

^aGenotype could not be determined in three animals.

^bGenotype could not be determined in one animal.

^cGenotype could not be determined in seven animals.

^dSex was genotyped in a subpopulation.

^eNo numbers are given for E13.5–E16.5, as an omphalocele is physiological until E16.5 and is present in all fetuses.

experiments were performed with E18.5 fetuses unless stated otherwise.

Down-regulation of CaD with siRNA in cell culture suggested that CaD deficiency affected cell migration (Jiang et al., 2010). Therefore, we explored migration of primary embryonic fibroblasts in a cell wound healing assay. Wound width (in pixels) was determined at four predefined locations using ImageJ software. The initial distances at time 0 between the cell borders were similar in KO and WT cells (Fig. 3 A). The hourly monitored migration was biphasic; an initially slow wound closure (slow phase) was followed by an accelerated migration (fast phase; Fig. 3, B and C). The initial slow phase had faster migration rates in KO fibroblasts than in WT fibroblasts. In the second phase, KO and WT fibroblasts migrated with a similar velocity (Fig. 3 C).

In line with those results, migration of myoblasts into the so-called primary body wall, and fusion of myoblasts into myotubes, appeared not grossly impeded. Thus, all layers of the secondary abdominal wall, i.e., the epidermis, the dermis, the interstitial connective tissue, and the five muscle pairs (panniculus carnosus, external and internal oblique muscles, and transversus and rectus abdominis) could be discerned in E17.5 WT, KO, and HET fetuses (Fig. 4; and Fig. S1, C–F), as expected at gestational ages >16.5 (Nichol et al., 2012). However, the panniculus carnosus appeared discontinuous and hypoplastic in KO (compare Fig. S1, A and B) and did not extend as far toward the ventral midline as in WT (arrows in Fig. 4; and Fig. S1, A and B). The transversus abdominis in KO was thinner than in WT, but myofibers could be discerned (Fig. S1, A and B). The interstitial connective tissue appeared less organized and less pronounced.

Histology and protein composition of the urinary bladder

Urinary bladders from E18.5 *Caldt*^{-/-} mice exhibited a normal macroscopic appearance and no obvious pathologies at the light-microscopy level (Fig. 5). The areas of the lumen and the different layers of the bladder wall did not differ between *Caldt*^{-/-} and *Caldt*^{+/+} fetuses (*n* = 4 per group; Fig. 5 C). In particular, the area of the well-developed detrusor muscle, which occupied the largest part of the bladder wall, was similar in *Caldt*^{-/-} and *Caldt*^{+/+} fetuses. The urinary bladder weight (Fig. 5 D) and the ratio of the bladder weight to body weight (Fig. 5 E) were similar in the three genotypes.

Next, we investigated whether ablation of CaD affected expression of proteins of the contractile machinery in E18.5 urinary bladders. The global protein expression pattern did not differ between genotypes (Fig. 6 A). The content of actin and myosin heavy chain was assessed in Coomassie-stained gels in both intact and chemically skinned preparations because mechanical experiments were performed in both. In intact urinary bladders from KO and WT, the actin (Fig. 6 B) and myosin (Fig. 6 C) content and the molar ratio of actin to myosin (Fig. 6 D) were similar. In skinned WT strips, there was a small loss of actin and myosin, but the actin-to-myosin ratio was not different from that in intact strips (Fig. 6, B–D). In contrast, in skinned KO, the contents of actin and myosin were significantly lower than in intact strips, whereby the loss of myosin exceeded that of actin (Fig. 6, B and C), so that the actin-to-myosin ratio was significantly higher in skinned KO compared with skinned WT (Fig. 6 D). The TM content relative to actin increased in KO strips (actin:TM decreased). Skinning lowered the actin-to-TM ratio in WT but not in KO strips (Fig. 6 E). Thus, both KO strips and

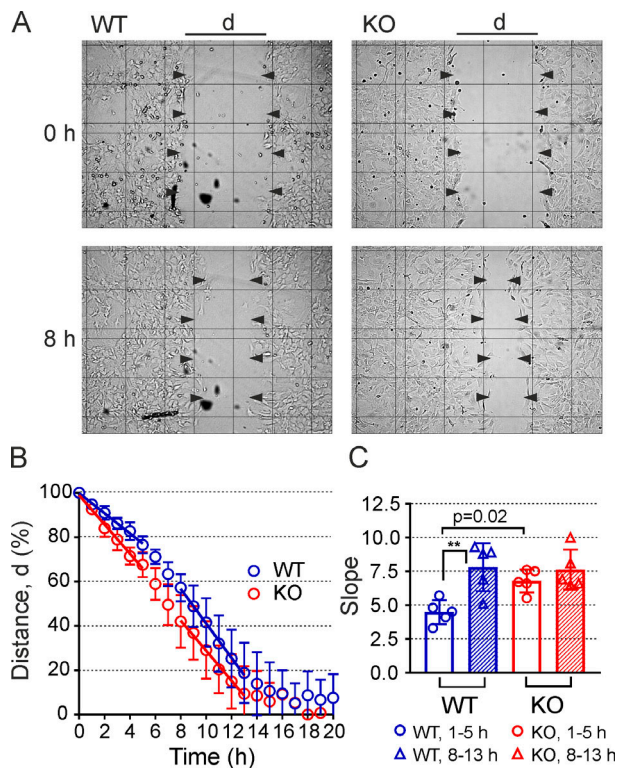


Figure 3. Migration of embryonic fibroblasts (E14.5 ± 0.5) assayed with a wound healing assay. (A) Example of cell wounds made by a 200- μ l pipette tip at time 0 and after 8 h; d, distance between borders of the cell layer. Closure of the wound was determined at four predetermined positions on each side (arrowheads). **(B)** Relative narrowing of the distance, d, given in percentage of initial distance at time 0 h. Symbols represent means \pm SD from four individual experiments per genotype; straight lines represent linear regression between 1–5 and 6–13 h. **(C)** Means \pm SD of the slopes (% closure/h) of the regression lines from the individual experiments ($n = 4$), showing that initial migration of KO was faster than that of WT. **, $P < 0.01$ (two-way ANOVA followed by Sidak’s multiple comparison posttest).

skinned WT strips had sufficient TM to saturate the actin filaments.

The content of nonmuscle myosin heavy chain IIA did not differ between genotypes in Western blots probed with anti-nonmuscle myosin heavy chain IIA antibodies (Fig. 6 F; ratio of nonmuscle myosin heavy chain/GAPDH 1.1 ± 0.4 in WT and 0.93 ± 0.2 in KO, $P = 0.57$). In skinned fibers, the nonmuscle myosin heavy chain IIA content was reduced by $\sim 40\%$ in WT and by $\sim 35\%$ in KO (Fig. 6 G). We did not normalize the nonmuscle myosin heavy chain signal, as skinning resulted in loss of GAPDH and SM22 (compare Fig. 6 F). No immunoreactivity was observed with antibodies directed against the other nonmuscle myosin heavy chain II isoforms.

The expression level of MLCK, the regulatory (MYPT1) and catalytic (PP1c δ) subunit of myosin light chain phosphatase (MLCP), and the MLCP inhibitory endogenous peptide, CPI-17, did not differ between WT and KO E18.5 intact bladders (Fig. 7, A–C). The expression of the actin binding proteins, calponin and fascin, which bundle actin filaments, was not different (Fig. 7, A and B). Phosphorylation of MYPT1 is a key regulator of MLCP activity. Phosphorylation was determined in nonstimulated

strips. Inhibitory phosphorylation of MYPT1 at T696 normalized to MYPT1 was higher in intact KO strips (Fig. 7, D and E). In skinned strips, it was significantly lower (pT696 WT intact versus WT skinned, $P > 0.01$; KO intact versus KO skinned, $P > 0.001$) but did not differ between KO and WT strips (Fig. 7, D and E). Phosphorylation levels of T853 were similar in intact and skinned KO and WT strips (Fig. 7, D and F).

Mechanical parameters in chemically skinned longitudinal strips from E18.5 urinary bladders

As the impact of CaD on smooth muscle contraction has been investigated in Triton S-100-skinned fibers (Pfitzer et al., 1993; Malmqvist et al., 1996; Albrecht et al., 1997; Pfitzer et al., 2005), we first investigated the contractile properties in such skinned strips from urinary bladder prestretched to $1.5L_0$ (Fig. 8). In contrast to CaD-extracted Triton X-100-skinned taenia coli fibers (Pfitzer et al., 2005), *Cald1*^{-/-} strips did not contract in the absence of Ca²⁺ (pCa > 8). The threshold pCa for eliciting a contraction was lower in KO than in WT ($P < 0.01$; Fig. 8 B). To obtain a full force–pCa relation from each preparation but limit rundown, we kept the duration of the experiments short by switching to the next higher pCa solution after 5 min, meaning that forces at low pCa had not yet reached steady state completely. The thus-obtained force–pCa relationship was shifted to the left in KO strips by 0.18 ± 0.04 pCa units ($P < 0.001$; Fig. 8 B). It is possible that this reflects a faster increase in force rather than an increased steady state. The pCa₅₀ value, which is the negative logarithm of the [Ca²⁺] at which 50% of maximal force is developed, is a measure of Ca²⁺ sensitivity. It was significantly higher in *Cald1*^{-/-} preparations compared with WT littermates (Fig. 8 C). The Hill coefficient of the force–pCa relations, n_H , did not differ between genotypes (3 ± 0.79 in WT, 3.4 ± 0.96 in KO; $P = 0.214$). Force at maximally activating [Ca²⁺] (pCa 4.3) was significantly lower in *Cald1*^{-/-} than in *Cald1*^{+/+} preparations, but contraction/relaxation cycles were reproducible during the course of the experiment (Fig. 8 A). By inhibiting MLCP with the phosphatase inhibitor, microcystin, we tested whether the reduced force was due to incomplete activation. Strips incubated with pCa 6.74 solution did not contract. Addition of microcystin (1 μ M) to this solution elicited a contraction similar to that elicited by pCa 4.3 in the absence of microcystin (106% in KO and 101% in WT, $n = 4$ fetuses each). The lag time before force started to rise was significantly larger in KO than in WT (KO: 132 ± 6 s, $n = 4$; WT: 79 ± 6 s, $n = 4$; $P = 0.014$). Increasing pCa to 4.3 at the plateau of the microcystin-induced contraction did not further increase force. Thus, the reduced force in KO was not due to incomplete activation. Relaxation induced by switching from pCa 4.3 to pCa > 8 solution was significantly slower in *Cald1*^{-/-} strips than in WT strips (Fig. 8, A and E).

RLC phosphorylation in chemically skinned longitudinal strips from E18.5 urinary bladders

While the lower content of myosin in skinned *Cald1*^{-/-} strips can explain the lower force, we hypothesized that a lower RLC phosphorylation might be a contributing factor. The experimental protocol was as in Fig. 9 A. Reactions were terminated either after a full contraction/relaxation cycle (relaxed) or at the

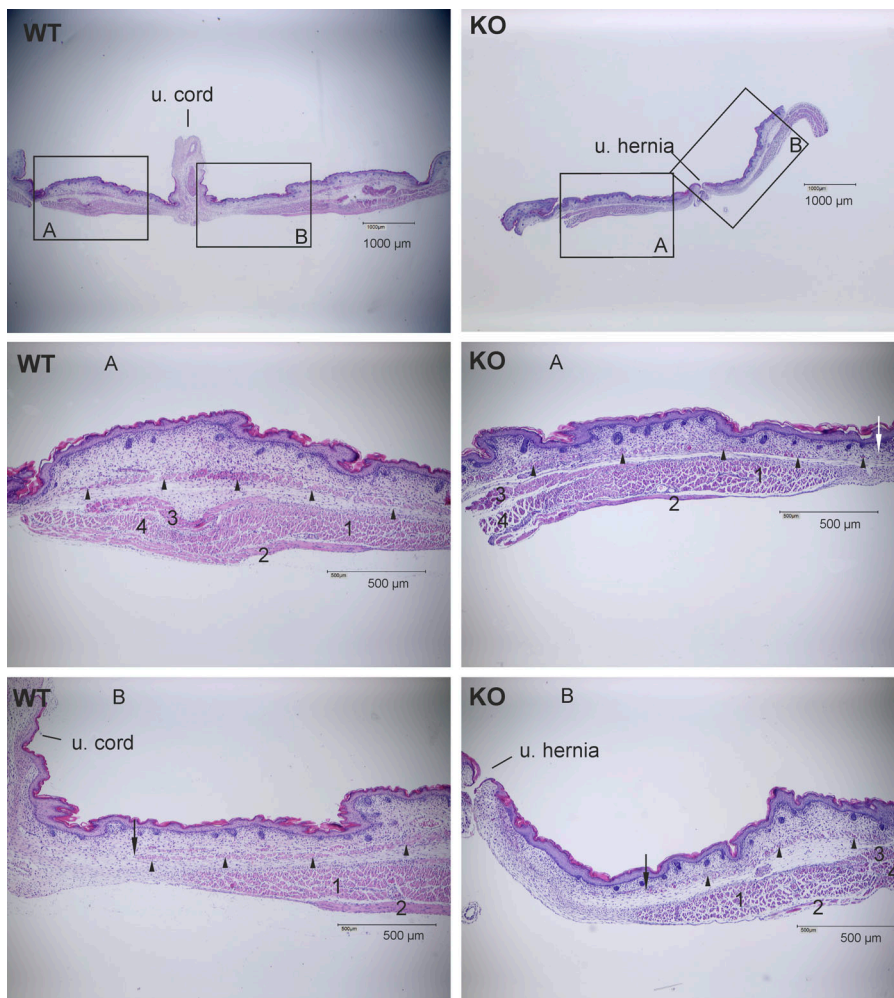


Figure 4. **Histology of the ventral abdominal wall of E17.5 fetuses.** All layers of the secondary wall were developed in WT (left panels) and KO (right panels). Magnification: 1.25 \times (A); 5 \times (B and C). u., umbilical. The content of the herniation was removed in this KO fetus; arrowheads indicate panniculus carnosus, which appeared discontinuous in KO and was further away from the midline compared with WT (arrows). 1, rectus abdominis; 2, transversus abdominis; 3, obliquus externus; 4, obliquus internus. Representative images of two *Cald1*^{+/+}, four *Cald1*^{-/-}, and two *Cald1*^{+/-} fetuses. Scale bars are incorporated in the figures.

plateau of the subsequent maximal contraction (pCa 4.3, contracted). In silver-stained 2-D-PAGE, two to three isoelectric variants of RLC were separated in relaxed strips and four in contracted strips, similar to adult smooth muscles (Fig. 9, A and B). In adult smooth muscles, these spots represent unphosphorylated smooth muscle RLC (smRLC), here denoted as U (the most basic spot in Fig. 9 A), monophosphorylated smRLC (denoted as P3), a mixture of diphosphorylated smRLC and unphosphorylated nonmuscle RLC (nmRLC; P2), and monophosphorylated nmRLC (P1, the most acidic spot in Fig. 9 A; Yuen et al., 2009; Puetz et al., 2012; Zhang and Gunst, 2017). A combination of 2-D Phos-Tag PAGE and Western blot analysis using phosphospecific antibodies against pS19 indicated that spot U represented unphosphorylated RLC. Furthermore, the intensity of U decreased upon activation (Fig. 9, C and D). In contracted, but not in relaxed, strips, spots P1-P3 contained phosphorylated RLC-S19 (Fig. 9 B). Thus, we are confident that the different spots represent the same isoelectric variants of RLC as in adult smooth muscle, although the relative distribution of the RLC variants differed. In particular, P3, representing monophosphorylated RLC, did not differ between relaxed and contracted fetal bladders (Fig. 9, C and D). In identically treated adult detrusor muscle, we observed the typical adult pattern, i.e., the signal intensity of P3 in silver-stained 2-D-

PAGE was low under relaxed conditions and much higher in contracted smooth muscle. Although none of the isoelectric RLC variants reacted with anti-pS19 antibodies in relaxed fetal strips, incubation with [γ ³²P]ATP at pCa >8 revealed phosphate turnover in spots P1-P3 (not depicted). Since cells in fetal bladders likely are dividing, it is possible that RLCs are phosphorylated at the N-terminal PKC sites known to be phosphorylated during mitosis (Totsukawa et al., 1996). This could account for the high phosphorylation of P3 at rest.

Important for the current investigation was that the overall pattern and signal intensities of RLC isoelectric variants were similar between *Cald1*^{-/-} and *Cald1*^{+/+} preparations under relaxed conditions. In contracted strips, however, P2, representing mainly double-phosphorylated smRLC, was lower in KO compared with WT strips ($P < 0.01$; Fig. 9 C). Consistent with this, U, representing unphosphorylated RLC, was higher in KO ($P = 0.01$). This suggests that the phosphorylation propensity was slightly less in KO, which may contribute to the observed lower Ca²⁺-activated force.

Biomechanics of intact bladder and aorta

In the next series of experiments, we evaluated the resting and KCl-stimulated force-length relation (Fig. 10), followed by testing the response to stimulation with carbachol (Fig. 11) in intact

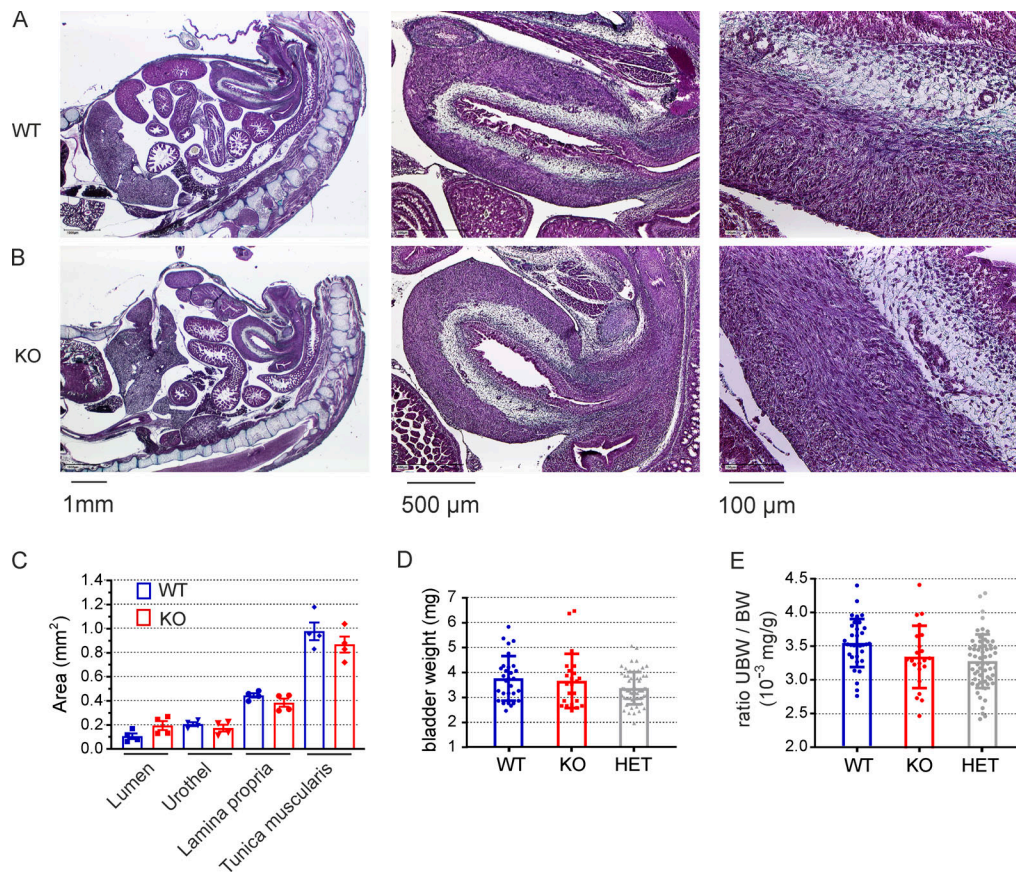


Figure 5. Histological sections, morphometry, and weight of E18.5 urinary bladders. (A and B) Representative images of WT (A) and KO (B) of Masson-Goldner-stained 7.5- μ m sagittal sections of whole embryo mounts at three different magnifications, showing the urinary bladder with the urothel, the lamina propria, and the tunica muscularis. Scale bars, which are incorporated in the figures, are also shown below the sections for better visibility. (C) In each fetus ($n = 4$ per genotype), three adjacent sections were analyzed and averaged; symbols represent the averaged values per fetus. Bars: mean \pm SD; no significant difference was observed. (D and E) Bladder weight (D) and ratio of urinary bladder weight (UBW) to body weight (BW; E) was not different between genotypes. Symbols and bars represent mean \pm SD.

fetal urinary bladder strips from *Cald1*^{+/+}, *Cald1*^{-/-}, and *Cald1*^{+/-} fetuses. In HETs, the CaD content was \sim 65% of that in WT (0.15 μ g/mg total protein in KO, $n = 12$, versus 0.23 μ g/mg total protein in WT, $n = 4$; $P = 0.07$, Mann-Whitney U test). The resting length-tension relation did not differ between the genotypes (Fig. 10 B). Interestingly, it was not possible to stretch the strips beyond 1.15 L_0 without damaging them. At all prestretches, the strips were stimulated with 80 mM KCl, which typically induced a biphasic contraction: an initial fast increase in force to a first peak (peak 1), was followed by a partial relaxation, and a second slower rise in force to a second peak (peak 2), from which the strips relaxed to a markedly lower steady-state level (Fig. 10 A). The amplitude of peak 1 relative to peak 2 was highly variable.

Force in WT increased with increasing lengths (Fig. 10, B-D). In KO, peak 1 force did not show a length-dependent increase and was lower than in WT at all prestretches, but the level of significance was reached only at 1.1 L_0 due to the high variability (Fig. 10 B). In HETs, peak 1 was higher than in WT at all prestretches, and most pronounced at 1.05 L_0 without reaching the level of significance (Fig. 10 B). The behavior of peak 2 was more complex. In WT, it increased with increasing lengths, whereas in KO and HET strips, it increased only with prestretching from

1.05 L_0 to 1.1 L_0 and decreased at 1.15 L_0 (Fig. 10 C). Plateau force at 1.15 L_0 was lower in HET and KO strips compared with WT (Fig. 10 D). The strips were then incubated with increasing concentrations of carbachol (Fig. 11). We found no significant differences, although force at 3 μ M carbachol tended to be lower in *Cald1*^{-/-} than WT (Fig. 11, A-C).

Next, we explored the effect of deletion of CaD in intact abdominal aorta (Fig. 11, D-G). The relation between passive force and radial stretching of ring preparations determined at the beginning of the experiment did not differ between aortas from *Cald1*^{-/-} and *Cald1*^{+/+} E18.5 fetuses (Fig. 11 E). In some preparations, tone increased during the equilibration period regardless of the genotype (Fig. 11 D). Resting force before incubation with U46619 tended to be lower in KO than in WT (2.9 \pm 0.5 mN in WT versus 1.9 \pm 0.3 mN in KO, $P = 0.07$). Maximal force (F_{max}) in the presence of 1 μ M U46619 was significantly lower in KO (5.0 \pm 0.4 mN in WT versus 3.6 \pm 0.4 mN in KO; $P = 0.032$; Fig. 11 G). The U46619 concentration-response curve was shifted to the right in *Cald1*^{-/-} aortae (Fig. 11 F). In three fetuses from each group, we obtained a second concentration response relation in the presence of L-NAME to test whether tone was attenuated by endothelial NO release. L-NAME increased neither resting

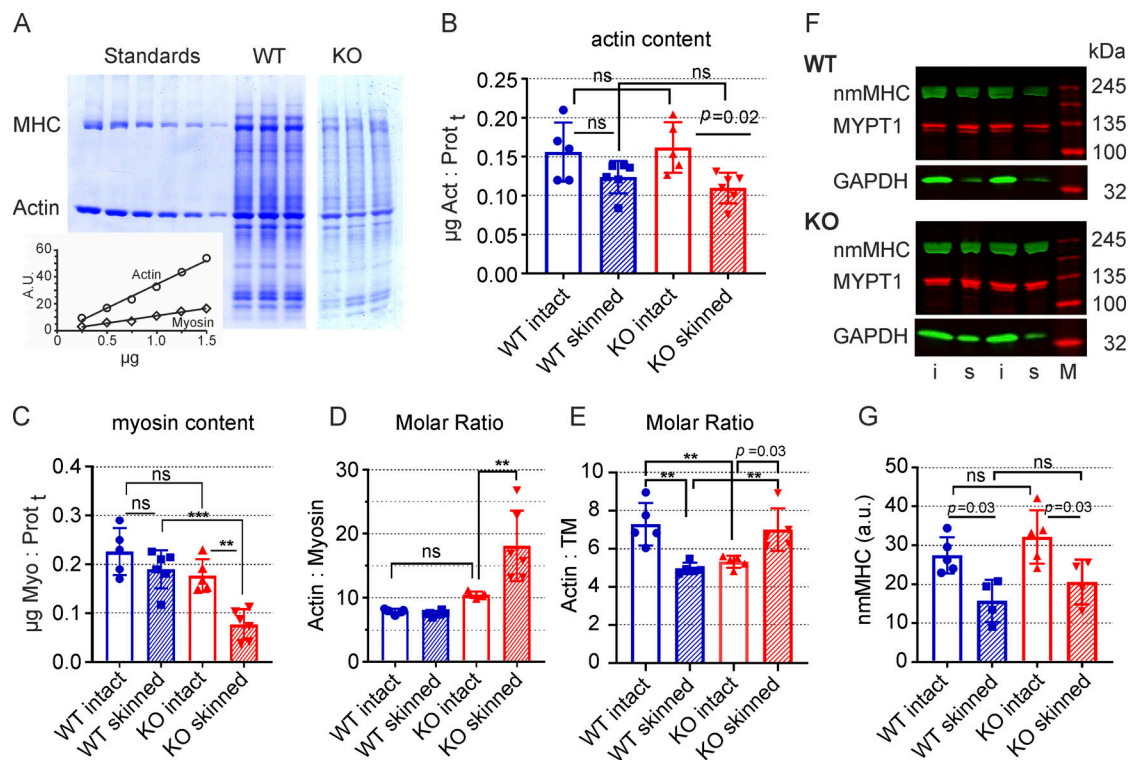


Figure 6. Myosin, actin, and nonmuscle myosin heavy chain content of E18.5 bladders. (A) Representative Coomassie-stained SDS-PAGE with skeletal actin and turkey gizzard myosin as standards, and lysates from three intact WT and KO bladders each from E18.5 fetuses. Insert: calibration curve. (B–E) Summary of results from intact and skinned bladder strips of actin (Act) content (B), myosin (Myo) content (C) relative to total protein (Prot_t), molar ratio of actin to myosin (D), and actin to TM (E), the molar ratio of actin:myosin in skinned KO is significantly higher than in WT. $P < 0.001$; symbols represent of intact (i) and skinned (s) urinary bladders; $n = 5$ fetuses per genotype. In these experiments, one half of the bladder was used intact, and the other half was skinned. Immunoreactivity was detected with the Odyssey system using IR680-conjugated (red) anti-mouse and IR800-conjugated (green) anti-rabbit secondary antibodies. (F) Representative Western blot probed with antibodies against nonmuscle myosin heavy chain IIA, MYPT1, and GAPDH from intact (i) and skinned (s) urinary bladders; $n = 5$ fetuses per genotype. In these experiments, one half of the bladder was used intact, and the other half was skinned. Immunoreactivity was detected with the Odyssey system using IR680-conjugated (red) anti-mouse and IR800-conjugated (green) anti-rabbit secondary antibodies. (G) Summary of densitometry (a.u., arbitrary units). Symbols represent the values from determination in one fetus; bars are mean \pm SD; MHC, myosin heavy chain; ns, not significant. **, $P < 0.01$; ***, $P < 0.001$ (two-way ANOVA, Sidak's multiple comparisons posttest).

tone nor F_{max} significantly regardless of genotype ($n = 3$; not depicted).

Discussion

Main findings

The primary goal of our study was to get more insight into CaD's in vivo function for regulation of smooth muscle contraction. To this end, we deleted both h-CaD and l-CaD by gene targeting to prevent one form from substituting for the other in functional assays. Given the widespread expression of l-CaD and its presumed role in a number of different cell functions, which likely are important for sustaining pregnancy as well as for embryonic/fetal development (Kilpatrick et al., 2009; Li et al., 2009; Paule et al., 2010), we were surprised to find that CaD appeared to be essential for neither embryogenesis nor for organogenesis, although HET pairing appeared to produce fewer pregnancies. In established pregnancies, Mendelian distribution was not violated, and the growth curves were normal until E17.5. No gross pathology of visceral organs was detected in E18.5 histological sections except for the persistence of the physiological umbilical hernia until birth with nearly 100% penetrance, an incompletely fused xiphoid process, and whitish spots at the surface of the

liver. In KO, the muscles of the abdominal wall appeared hypoplastic and dysmorphic. The persistence of the physiological umbilical hernia is the conspicuous cause of perinatal death and maternal cannibalism. From this, we concluded that CaD is essential for the relocation of the intestine from outside of the abdomen, where it develops until ~E16 in mice, into the abdominal cavity, and the closure of the umbilical ring around the umbilical cord. HET mice were viable and had no overt pathological phenotype and a normal life span. To minimize suffering of the homozygous mice during delivery, pregnancies were terminated by E18.5–E19.5. At this stage, fetal urinary bladder is fully contractile and more mature than other smooth muscles such as aorta (Arens et al., 2000). This allowed us to pursue our primary goal, namely exploring the role of CaD for smooth muscle contraction, as is discussed next.

Effect of CaD depletion on contractile function of fetal bladders

Despite their well-known limitations, Triton X-100–skinned smooth fibers have been widely used as a valuable tool to analyze the mechanical properties of the contractile machinery without interference of membrane ion fluxes (Pfitzer and Boels, 1991). This preparation allowed us to relate our results to

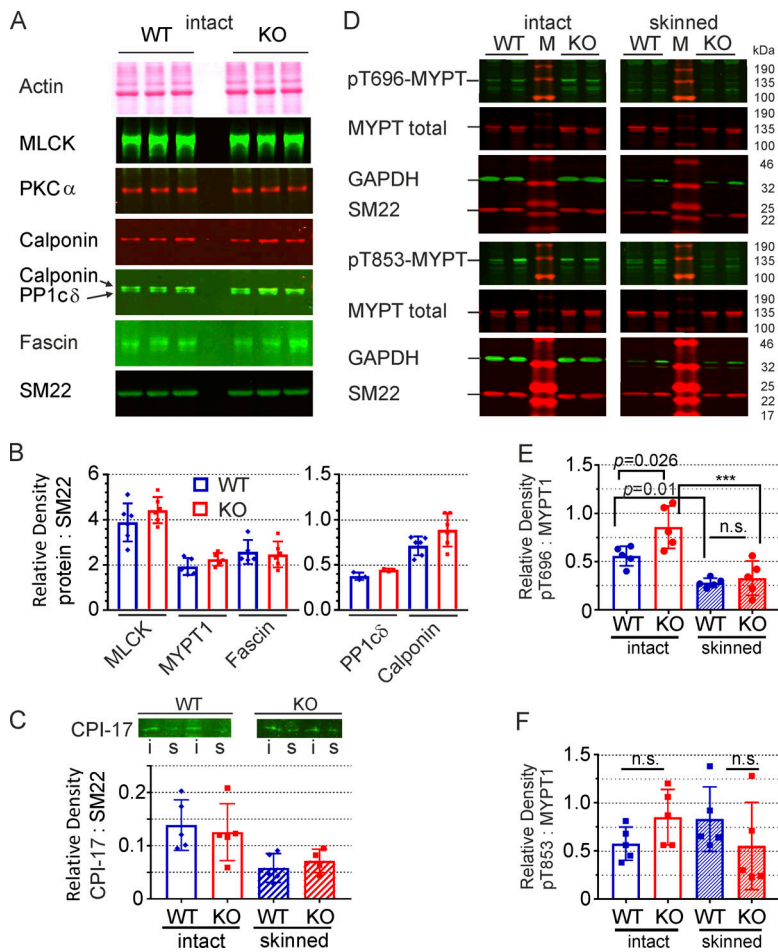


Figure 7. Western blot analysis of regulatory proteins in *Cald1*^{+/+} (WT) and *Cald1*^{-/-} (KO) bladders from E18.5 animals. (A) Representative Western blots: proteins of lysates were separated by 4–20% SDS-PAGE and transferred to nitrocellulose. The membranes were sequentially probed with the respective primary antibodies; immunoreactivity was visualized as in Fig. 6. Both SM22 (Western blot) and actin (Ponceau red stain of nitrocellulose membrane) were used as loading controls. (B) Summary of results of five to six determinations (one per fetus). Note different scales of y axis; there were no significant differences for the respective proteins between genotypes. (C) Expression of CPI-17 in intact and skinned fibers and summary of results; i, intact; s, skinned; CPI-17 diffuses out of skinned fibers. (D) Representative Western blots with phosphor-specific antibodies against phosphorylation of MYPT1 at T696 (pT696-MYPT1, upper panels) and T853 (pT863-MYPT1, lower panels), and antibodies against MYPT1 total in intact and skinned bladder strips; GAPDH and SM22 were used as loading controls. M, molecular weight marker proteins. (E and F) Summary of results; symbols represent individual fetuses (five KO and five WT fetuses from a total of five litters; bladders were split in half; one was homogenized intact, and the other after skinning). Bars represent means \pm SD; n.s., not significant. ***, $P < 0.001$.

previous reports (Pfitzer et al., 1993; Malmqvist et al., 1996; Albrecht et al., 1997; Pfitzer et al., 2005). In our experiments, Ca^{2+} sensitivity in KO skinned bladder strips was increased by ~ 0.2 pCa₅₀ units, corroborating previous experiments, in which CaD was extracted from skinned taenia coli (Malmqvist et al., 1996). The leftward shift of the force-pCa relation was reversed in the extracted strips by reconstitution with exogenous CaD (Malmqvist et al., 1996; Pfitzer et al., 2005). The magnitude of the shift (~ 0.1 pCa units) in the extracted/reconstituted fibers (Malmqvist et al., 1996) was similar to that in *Cald1*^{-/-} strips, but whether this is coincidental is unknown. Thus, our results suggest that CaD decreases Ca^{2+} sensitivity. This is consistent with increased uterine CaD expression during pregnancy leading to decreased Ca^{2+} sensitivity (Li et al., 2009). In contrast to our results, depletion of h-CaD had no effect on Ca^{2+} sensitivity of skinned aorta, but as in our study, relaxation was slower in response to lowering the free Ca^{2+} concentration (Guo et al., 2013). The notion that the slowed relaxation is related to CaD deficiency is supported by experiments in which loading of skinned fibers with CaD increased the rate of relaxation (Albrecht et al., 1997). Other causes for increased Ca^{2+} sensitivity or slowed relaxation, such as decreased activity of MLCP or increased nonmuscle myosin heavy chain expression, were unlikely, as we found no changes in these proteins in KO compared with WT mice (compare Figs. 6 and 7).

Relaxation started when MLCK was inactivated by lowering of [Ca²⁺], and RLC was dephosphorylated by MLCP. However, in

skinned fibers, dephosphorylation of RLC and the decay in ATPase activity generally is much faster than the force decay (Driska et al., 1989; Butler et al., 1990; Kühn et al., 1990), a condition that was related to the latch-like state of smooth muscle (Khromov et al., 1995). The slow force decay is governed by the slow detachment rate of dephosphorylated cross-bridges and/or cooperative reattachment of dephosphorylated cross-bridges (Khromov et al., 1995). Studies in skinned fibers suggested that CaD increased the rate of relaxation by inhibiting cooperative binding of dephosphorylated cross-bridges (Albrecht et al., 1997), a notion supported by experiments in solution (Hemric and Chalovich, 1988; Horiuchi and Chacko, 1989; Chalovich et al., 1998), although effects on product release are also a possibility (Lash et al., 1986; Marston, 1988; Ansari et al., 2008). CaD deficiency, in turn, would permit additional cross-bridge binding, which would lead to an increase in force-producing cross-bridges. Such cross-bridges would tend to activate the actin filament, increase the Ca^{2+} sensitivity, and decrease the rate of relaxation.

We did not observe a Ca^{2+} -independent contraction unless MLCP was inhibited by microcystin in KO skinned fibers. Moreover, there was no increase in resting force in intact E18.5 KO bladder strips and aorta. This behavior of fetal smooth muscle differs from adult smooth muscle. Interventions in the latter, which have in common that they lowered CaD's inhibitory effect, resulted in increased contractile activity at low levels

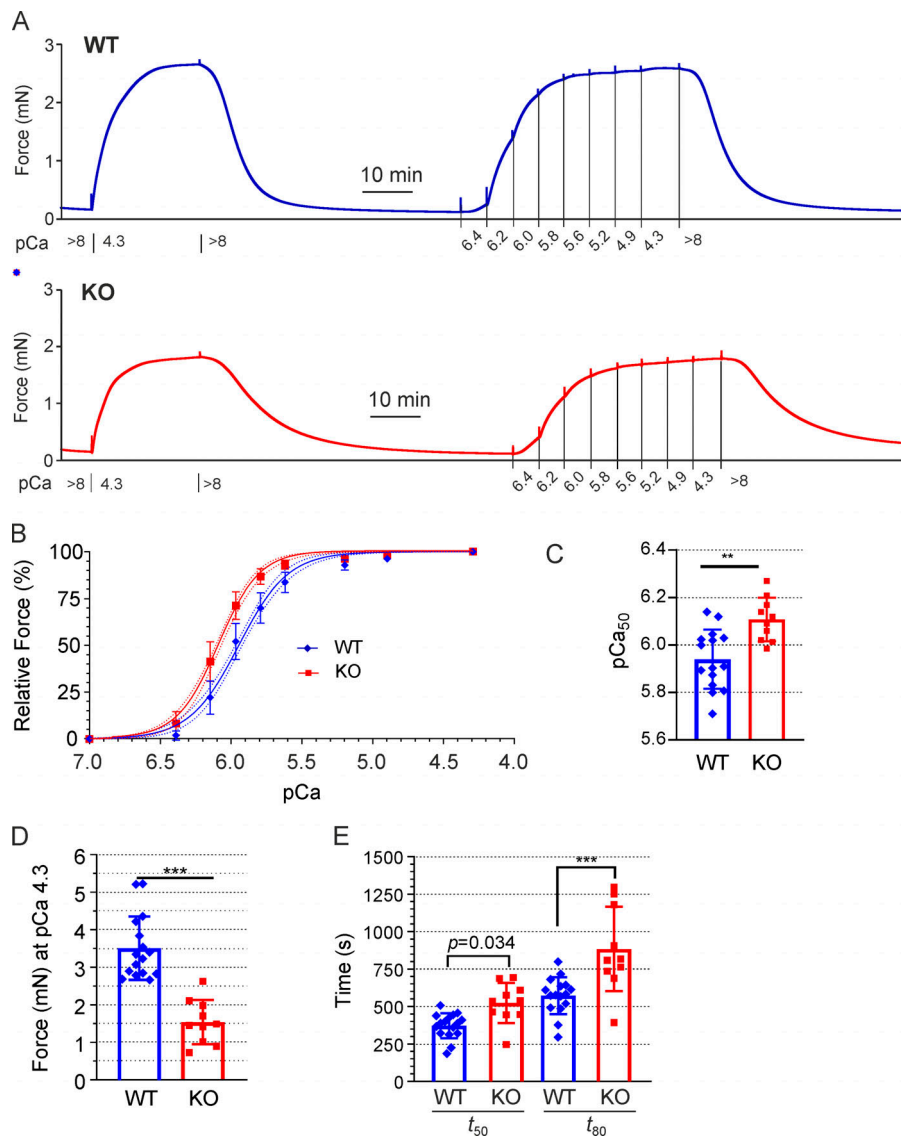


Figure 8. Force-pCa relationships and time course of relaxation in Triton X-100-skinned E18.5 urinary bladder strips. (A) Original force tracings of the experimental protocol. Following a test relaxation-contraction-relaxation cycle, isometrically mounted longitudinal strips were stimulated with cumulatively increasing pCa = $-\log[\text{Ca}^{2+}]$ for 5 min at each pCa. (B) Normalized force-pCa from $n = 23$ WT (*Cald1*^{+/+}) strips from 16 fetuses and 16 strips from 10 KO (*Cald1*^{-/-}) fetuses from a total of 13 litters; the results from both bladder halves of one fetus were averaged, when applicable, and the mean was taken for further calculation. Solid and broken lines represent nonlinear fit with a sigmoidal function and 95% confidence intervals of the force-pCa relations, respectively. Force at pCa 4.3 (F_{max}) was taken as 100%, and force at pCa >8 was taken as 0 (symbols represent mean \pm SEM). (C) Summary of pCa₅₀ values (pCa for 50% activation) taken from sigmoidal fits of individual experiments. (D) Maximal force at pCa 4.3 was significantly lower ($P < 0.001$) in KO than in WT. (E) Time required for 50% (t_{50}) and 80% (t_{80}) relaxation from F_{max} . Symbols represent values from individual fetuses, and bars are means \pm SD. **, $P < 0.01$; ***, $P < 0.001$.

of RLC phosphorylation (Katsuyama et al., 1992; Earley et al., 1998; Van Eyk et al., 1998; Pfitzer et al., 2005; Li et al., 2009). In turn, up-regulation of CaD in the pregnant uterus was associated with silencing of uterine contractility and was proposed to prevent premature contractions (Li et al., 2009). Interestingly, we noticed a tendency for premature birth close to term in KO. Taken together, these results support the idea that CaD acts as a molecular brake on contraction, regulated by CaD's phosphorylation state (Wang, 2001). This keeps the muscle relaxed at low RLC phosphorylation levels, preventing unwanted contractions.

The increased KCl-induced force in intact HET bladder strips is in line with such inhibitory properties of CaD. Not consistent with this notion is the observed attenuation of absolute force in smooth muscles from KO fetuses. The observation that CaD depletion attenuated force is not new. Such an effect has been reported in adult arteries in which CaD was down-regulated by siRNA (Earley et al., 1998) and in h-CaD KO mice (Guo et al., 2013). The authors of those studies proposed that the attenuated KCl-induced force was related to the observed increased resting

force. Alternatively, we propose that the lower force in KO is related to the known effects of CaD on the stability of actin (Castellino et al., 1992; Wang, 2008; Mayanagi and Sobue, 2011) and myosin (Katayama et al., 1995; Kudryashov et al., 2002) filaments.

The idea that CaD in smooth muscle contributes to filament stability came from our observation that the lower force in skinned KO strips coincided with a significantly lower myosin content compared with WT. This was not due to lower expression levels, as the content of both proteins did not differ between intact KO and WT bladders. Rather myosin and actin monomers diffused out of skinned fibers, a well-known limitation of Triton X-100-skinned smooth muscle (Pfitzer and Boels, 1991). The loss of actin and myosin in WT skinned strips was similar to previous reports. Unexpectedly, however, the loss of myosin was much larger in KO than in WT skinned fibers (~60% versus ~20%) and exceeded that of actin by far (compare Fig. 6). CaD, but also telokin, promote myosin filament formation in solution (Katayama et al., 1995; Kudryashov et al., 2002). They may, therefore, promote myosin filament stability in smooth muscle

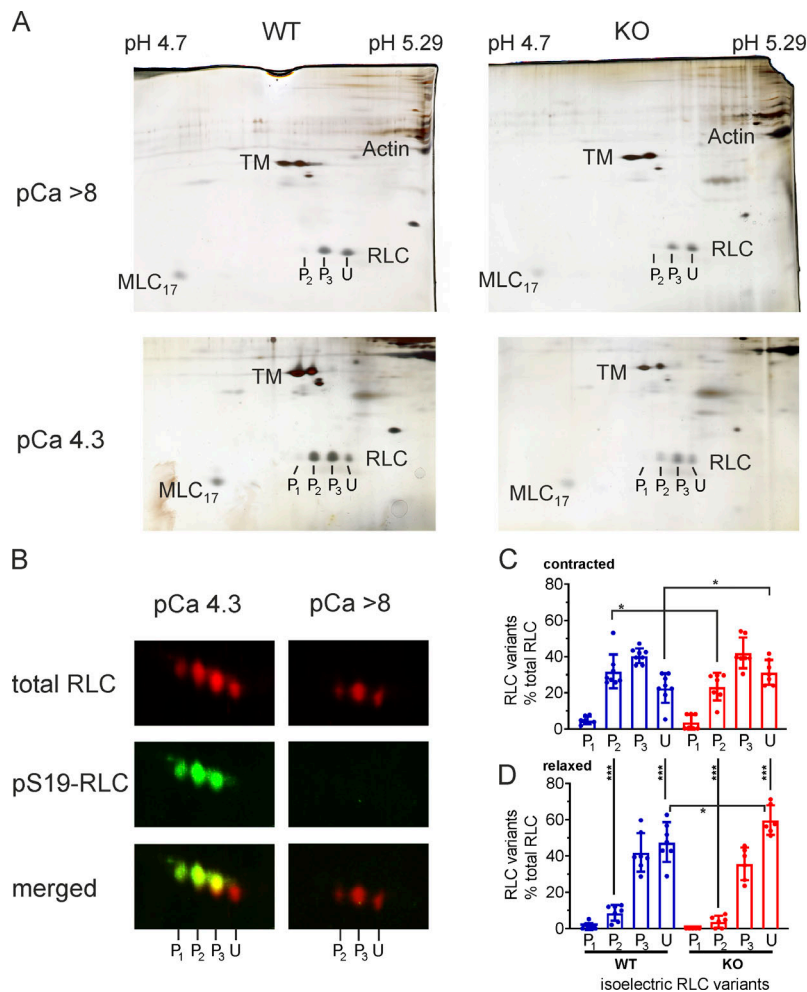


Figure 9. Phosphorylation of RLCs in relaxed (pCa >8) and stimulated (pCa 4.3) skinned bladder strips. Iso-metrically mounted strips underwent the same experimental protocol as in Fig. 8. The strips were fixed in TCA either after a full contraction/relaxation cycle (pCa >8, relaxed) or at the plateau of the subsequent maximal contraction (pCa 4.3, contracted). **(A)** Representative silver-stained 2-D-PAGE. MLC17, 17-kD light chain; U, unphosphorylated smooth muscle RLC (smRLC); P₁, monophosphorylated nmRLC; P₂, unphosphorylated nmRLC + diphosphorylated smRLC; P₃, monophosphorylated smRLC. **(B)** Phos-Tag 2-D-PAGE followed by Western blots with antibodies against RLC and RLC phosphorylated at S19. **(C and D)** Summary of results of densitometry of silver-stained 2-D-PAGE. RLC isoelectric variants were expressed in percentage of total RLC (sum of P₁, P₂, P₃, and U). Bars represent mean ± SD, and symbols are individual fetuses (relaxed: seven WT and six KO; contracted: eight WT and seven KO). *, P < 0.05; ***, P < 0.001 (comparison between genotypes, two-way ANOVA; contracted versus relaxed within one group with one-way ANOVA, both followed by Sidak's multiple comparison test).

tissue, which is particularly important at low levels of RLC phosphorylation, when myosin filaments remain in smooth muscle cells (e.g., Devine and Somlyo, 1971) but are destabilized in solution. Skinned fibers are devoid of telokin (Shcherbakova et al., 2010), so KO strips are devoid of both proteins, and this may explain the much larger loss of myosin in skinned KO compared with WT strips. Thus, the seeming disadvantage of skinned fibers unmasked the importance of CaD for stabilization of myosin filaments in smooth muscle.

We also observed a reduction of force in intact bladder and aorta from KO fetuses, albeit to a lesser extent. This was not surprising, as contractile proteins were not reduced in intact bladder. KCl-induced contraction was attenuated, especially in stretched KO preparations (cf. Fig. 10), suggesting that CaD stabilizes the contractile apparatus especially at long lengths, perhaps by tethering actin to myosin filaments (Marston et al., 1992). Unfortunately, it was not possible to directly test this idea, because the conservation of the contractile apparatus was not sufficient to determine filament density and filament spacing in EM (cf. Fig. S2). In this context, it is interesting to note that point mutations in the C terminus of CaD in a mouse model, which did not lower CaD expression levels but interfered with the inhibition on cross-bridge cycling, increased force (Deng et al., 2013) similar to the observed increased force in HETs in our study.

Numerous studies have demonstrated the involvement of CaD in regulation of the highly dynamic actin cytoskeleton in cultured cells including smooth muscle cells (e.g., Jiang et al., 2010). Compared with nonmuscle cells, actin and myosin filaments are much more stable in smooth muscle. Still, there is a small pool of G:F actin that changes upon mechanical and chemical stimulation, at least in some smooth muscles (Mauss et al., 1989; Gunst and Zhang, 2008; Yamin and Morgan, 2012; Moreno-Domínguez et al., 2013; Schubert et al., 2017). The state and organization of myosin in fetal bladder is not known, and thus its role in the altered contractility remains to be investigated. It was proposed that the regulation of the G:F actin balance occurs mainly at the cell membrane (Gunst and Zhang, 2008). The subcortical G:F actin balance controls ion channel activity of, e.g., piezo channels (Morachevskaya and Sudarikova, 2021). This gives rise to the interesting possibility that CaD affects excitation contraction by affecting subcortical actin remodeling, another possibility that could explain lower force in our stretched preparations.

Effect of CaD depletion on abdominal wall closure

The most conspicuous phenotype, however, with near-100% penetrance, was the giant omphalocele, which was extremely rare in WT. During normal development in humans and mice,

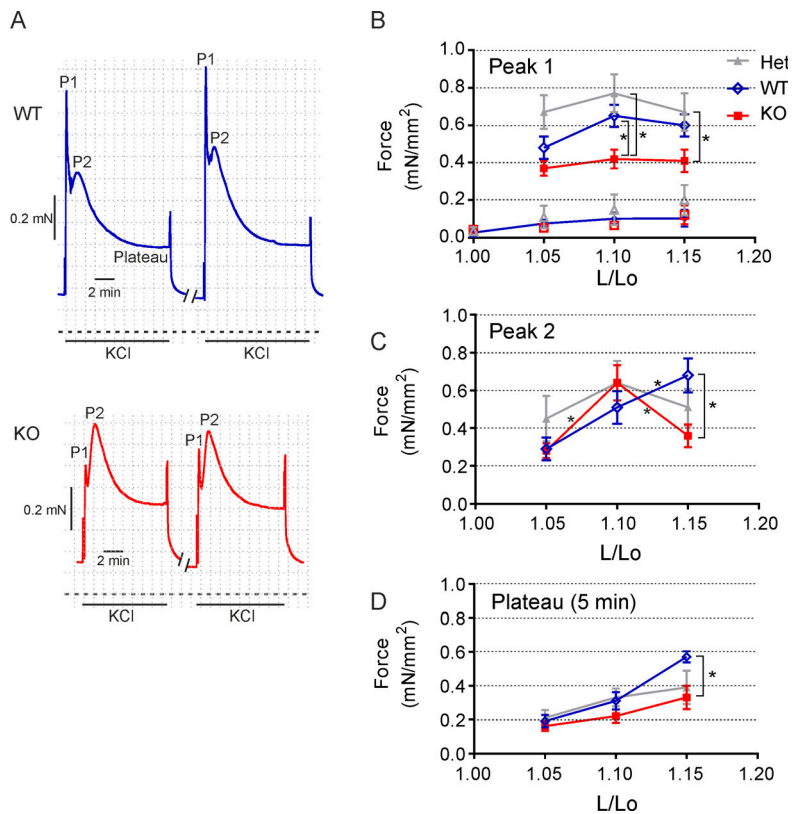


Figure 10. **Length dependence of resting and KCl-induced force in WT, KO, and HET intact urinary bladder strips.** (A) Original force tracings of 80 mM KCl elicited force at 1.1L₀. In the majority of WT strips, KCl elicited a biphasic contraction; P1, peak 1; P2, peak 2. (B–D) Summary of results. The plateau force was determined 5 min after addition of KCl. Symbols represent mean ± SEM from 10 WT, 13 KO, and 9 HET bladder strips (1 per fetus) taken from 8 litters. *, P < 0.05 (two-way ANOVA, Sidak’s multiple comparisons test).

the gut herniates through the umbilical ring into the umbilical cord, where it develops within a mesodermal sac (physiological umbilical herniation) while being attached at the dorsal abdominal wall through the mesentery. Relocation of the gut into the abdominal cavity and closure of the umbilical ring around the umbilical cord is completed by E16.5 in mice (Brewer and Williams, 2004). Herniation of the gut was also observed in h-CaD-deficient offspring but with a lower penetrance (Guo et al., 2013). Those that had no hernia survived into adulthood. From that we conclude that l-CaD is essential for resolution of the physiological hernia.

The occurrence of an omphalocele is frequently associated with pulmonary problems (Carnaghan et al., 2013). To date, nothing is known about the role of CaD in lung development. It is interesting to note that an omphalocele in conjunction with delayed maturation of the alveolar structure was observed in a mouse model with targeted depletion of the glucocorticoid receptor (Li et al., 2013), which is known to regulate transcription of CaD (Mayanagi and Sobue, 2011). CaD expression was not investigated in that mouse model. In our model, maturation of the alveolar space appeared to be only slightly delayed (cf. Fig. 2), if at all. We are currently exploring this in more detail.

The prevalence of an omphalocele in humans is ~1 in 4,000 live births. It frequently coexists with a wide variety of other nonoverlapping malformations (Conner et al., 2018). The underlying causes are multifactorial and can be genetic and environmental (reviewed in Brewer and Williams, 2004). The highly complex mechanisms that orchestrate the relocation of the gut into the abdominal cavity and closure of the abdominal wall are as yet poorly understood (Bargy and Beaudoin, 2014). Targeting

a wide variety of genes in model organisms (reviewed in Brewer and Williams, 2004), some of which code for proteins involved in contractile mechanisms (Shimizu et al., 2005; Ma and Adelstein, 2014; Chen et al., 2015), caused abdominal wall defects of variable size. Those were often associated with additional malformations (e.g., Ma and Adelstein, 2014). As it was hardly ever specified whether the defect was an omphalocele or a gastroschisis, two entirely different entities, comparisons between these models are difficult (Carnaghan et al., 2013). Nevertheless, an impaired organization of the epithelial actin cytoskeleton was common to some of these models (Nichol et al., 2011). This resulted in an arrest in the development of the so-called secondary abdominal wall, the development of which starts at ~E11.5 and is completed by E14.5, and involves migration of mesenchymal cells and myoblasts into the primary body wall (cf. Nichol et al., 2012).

CaD was implicated in C1C12 myoblast migration and differentiation (Jang et al., 2013). In contrast to these cell culture data, migration of myoblasts appeared not to be impeded in *Caldl*^{-/-} mice. This is not surprising, as embryonic fibroblast migration was not impaired in our experiments. In fact, all structures and patterning of the secondary abdominal wall, including the five principal muscles and the orientation of the myotubes within the different muscles, were present. However, the muscles appeared hypoplastic, and the panniculus carnosus was discontinuous and stopped further away from midline than in WT. How those changes relate to the omphalocele is currently not clear. Most studies focused on the abdominal wall. However, a recent study demonstrated that inhibition of bone morphogenetic protein activity resulted in

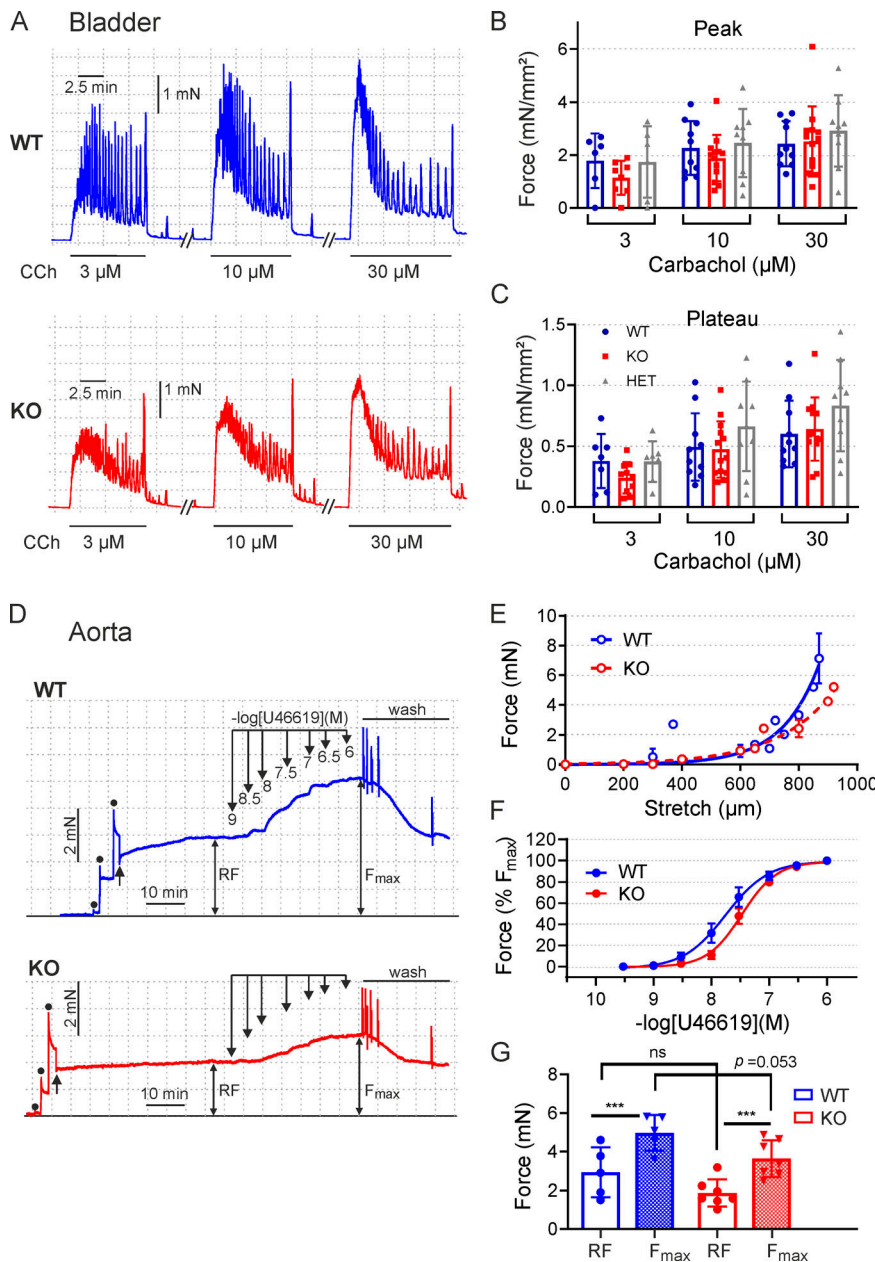


Figure 11. Contractile parameters in intact E18.5 urinary bladder aorta. At the end of the protocol shown in Fig. 10, the bladder strips were stimulated with increasing concentrations of carbachol (CCh) at $L = 1.5L_0$. **(A)** Original force tracings of a WT and a KO urinary bladder strip; force responses in HET were similar (not depicted). **(B and C)** Summary of results. Peak denotes the initial maximal tonic response, and plateau, the tonic response after 5-min stimulation. Bars represent mean \pm SD (symbols represent determinations from individual fetuses; cf. Fig. 10). Force in KO elicited by 3 μ M CCh tended to be lower in KO, and in HET at 10 and 30 μ M CCh higher than in WT, without reaching the level of significance. **(D)** Original force tracings from ring preparations of the abdominal aorta, which shows the force response to stepwise stretching (dots) and release to IC_{90} (upward arrow) according to the Mulvany normalization protocol (see Materials and methods). RF, resting force before addition of U46619, and the response to increasing concentrations of U46619. **(E)** Relation between force and stretch during normalization protocol ($n = 3$ WT and $n = 3$ KO fetuses). **(F)** U46619 concentration-response curve. Symbols represent mean \pm SEM, and lines represent the sigmoidal fits, which are significantly different between groups. **(G)** Summary of resting force (RF) before application of U46619, and F_{max} = total force. Symbols represent force responses from five WT and seven KO fetuses from five litters (one preparation per animal). Bars: mean \pm SD; n.s., not significant ($P = 0.07$); ***, $P < 0.001$ (two-way ANOVA, uncorrected Fisher's least significant difference posttest).

altered actin cytoskeleton of mesenchymal cells and biomechanics of the mesentery along with an omphalocele (Nerurkar et al., 2017). Thus, it is possible that the mesentery, which is a highly elastic structure (Savin et al., 2011), is involved in retraction of the gut before the abdominal wall can close. This possibility has been little explored, to our knowledge. In that context, it is of interest that a point mutation of the regulatory subunit of MLCP, MYPT1^{T696A}, also presented an omphalocele, although the underlying mechanism was not explored (Chen et al., 2015). This gives rise to the possibility that contractile processes may be involved. It is thus possible that CaD affects abdominal wall closure by regulating reorganization of the actin cytoskeleton in epithelial cells and by modulating the biomechanics of the mesentery. Unraveling the mechanisms by which deletion or mutation of contractile

proteins interfere with body wall closure will contribute to our comprehension of the ventral body wall development.

To summarize, we propose that CaD has a dual function for the regulation of smooth muscle contraction. First, it acts as a molecular brake on smooth muscle contraction by inhibiting cross-bridge cycling, especially at low levels of RLC phosphorylation, a finding that corroborates previous reports. Second, it serves as a structural protein, which, perhaps in conjunction with other proteins, maintains the structural integrity of the contractile apparatus. A limitation of our study is that we could not investigate the effect of CaD ablation only in fetal smooth muscle. However, we believe that our results apply to adult smooth muscle, given that fetal bladder is rather mature in midterm fetuses. Finally, the novel and, in our view, most important observation of our study is the finding that l-CaD is

indispensable for the resolution of the physiological umbilical hernia.

Acknowledgments

Henk L. Granzier served as editor.

The authors thank Dr. Veronika Hasse, Institute of Vegetative Physiology, University of Cologne for assistance with generation of the CaD antibody. The valuable advice of Prof. Dr. Angelika Noegel and Dr. V. Peche, and the support of Prof. Dr. Krieg, Prof. Dr. Wodarz, and Prof. Dr. Sengle (all University of Cologne) are gratefully acknowledged, as is the excellent technical assistance of Nadin Piekarek, Petra Müller, Cornelia Kock-Hauser, Maria Bust, Tim van Beers, Stephanie Naumann, Semra Özçelik, and Anja Kahl. We also thank the head of the animal housing facility of the Medical Faculty, Prof. Dr. E. Mahabir-Brenner, and her team for the excellent care of our mice.

This work was supported by funds of the Center for Molecular Medicine, University of Cologne, and the Medical Faculty (Koeln Fortune) of the University of Cologne to G. Pfützer, and by the Deutsche Forschungsgemeinschaft (FOR2722 to M. Koch).

The authors declare no competing financial interests.

Author contributions: S. Pütz designed and cloned the targeting vector and edited the manuscript. L.S. Barthel performed biomechanical and 2-D-PAGE experiments and analyzed data. M. Frohn performed histological experiments, genotyped the mice, analyzed data and edited the manuscript. D. Metzler supervised the breeding, conducted 2-D-PAGE and Western blotting, and analyzed data. M. Barham conducted light and electron microscopy and interpreted data. L.T. Lubomirov interpreted biomechanical data and edited the manuscript. G. Prymachuk conducted light microscopy and edited the manuscript. O. Trunschke genotyped the mice. J. Hescheler edited the manuscript. W.F. Neiss interpreted data and edited the manuscript. W.F. Neiss, M. Koch, M.M. Schroeter, and G. Pfützer supervised research in their respective laboratories. G. Pfützer wrote the manuscript with contributions from M.M. Schroeter and J.M. Chalovich.

Submitted: 29 September 2020

Accepted: 21 April 2021

References

- Abrams, J., G. Davuluri, C. Seiler, and M. Pack. 2012. Smooth muscle caldesmon modulates peristalsis in the wild type and non-innervated zebrafish intestine. *Neurogastroenterol. Motil.* 24:288–299. <https://doi.org/10.1111/j.1365-2982.2011.01844.x>
- Albrecht, K., A. Schneider, C. Liebetrau, J.C. Rüegg, and G. Pfützer. 1997. Exogenous caldesmon promotes relaxation of guinea-pig skinned taenia coli smooth muscles: inhibition of cooperative reattachment of latch bridges? *Pflugers Arch.* 434:534–542. <https://doi.org/10.1007/s004240050433>
- Ansari, S., M. Alahyan, S.B. Marston, and M. El-Mezgueldi. 2008. Role of caldesmon in the Ca²⁺ regulation of smooth muscle thin filaments: evidence for a cooperative switching mechanism. *J. Biol. Chem.* 283: 47–56. <https://doi.org/10.1074/jbc.M706771200>
- Arens, Y.H., C.R. Rosenfeld, and K.E. Kamm. 2000. Maturation differences between vascular and bladder smooth muscle during ovine development. *Am. J. Physiol. Regul. Integr. Comp. Physiol.* 278:R1305–R1313. <https://doi.org/10.1152/ajpregu.2000.278.5.R1305>
- Bargy, F., and S. Beaudoin. 2014. Comprehensive developmental mechanisms in gastroschisis. *Fetal Diagn. Ther.* 36:223–230. <https://doi.org/10.1159/000360080>
- Brewer, S., and T. Williams. 2004. Finally, a sense of closure? Animal models of human ventral body wall defects. *BioEssays.* 26:1307–1321. <https://doi.org/10.1002/bies.20137>
- Brozovich, F.V., C.J. Nicholson, C.V. Degen, Y.Z. Gao, M. Aggarwal, and K.G. Morgan. 2016. Mechanisms of Vascular Smooth Muscle Contraction and the Basis for Pharmacologic Treatment of Smooth Muscle Disorders. *Pharmacol. Rev.* 68:476–532. <https://doi.org/10.1124/pr.115.010652>
- Butler, T.M., M.J. Siegman, S.U. Mooers, and S.R. Narayan. 1990. Myosin-product complex in the resting state and during relaxation of smooth muscle. *Am. J. Physiol.* 258:C1092–C1099. <https://doi.org/10.1152/ajpcell.1990.258.6.C1092>
- Carnaghan, H., T. Roberts, D. Savery, F.C. Norris, C.J. McCann, A.J. Copp, P.J. Scambler, M.F. Lythgoe, N.D. Greene, P. Decoppi, et al. 2013. Novel exomphalos genetic mouse model: the importance of accurate phenotypic classification. *J. Pediatr. Surg.* 48:2036–2042. <https://doi.org/10.1016/j.jpedsurg.2013.04.010>
- Castellino, F., J. Heuser, S. Marchetti, B. Bruno, and A. Luini. 1992. Glucocorticoid stabilization of actin filaments: a possible mechanism for inhibition of corticotropin release. *Proc. Natl. Acad. Sci. USA.* 89:3775–3779. <https://doi.org/10.1073/pnas.89.9.3775>
- Chalovich, J.M., A. Sen, A. Resetar, B. Leinweber, R.S. Fredricksen, F. Lu, and Y.D. Chen. 1998. Caldesmon: binding to actin and myosin and effects on elementary steps in the ATPase cycle. *Acta Physiol. Scand.* 164:427–435. <https://doi.org/10.1046/j.1365-201X.1998.00449.x>
- Chen, C.P., X. Chen, Y.N. Qiao, P. Wang, W.Q. He, C.H. Zhang, W. Zhao, Y.Q. Gao, C. Chen, T. Tao, et al. 2015. In vivo roles for myosin phosphatase targeting subunit-1 phosphorylation sites T694 and T852 in bladder smooth muscle contraction. *J. Physiol.* 593:681–700. <https://doi.org/10.1113/jphysiol.2014.283853>
- Conner, P., J.H. Vejde, and C.M. Burgos. 2018. Accuracy and impact of prenatal diagnosis in infants with omphalocele. *Pediatr. Surg. Int.* 34: 629–633. <https://doi.org/10.1007/s00383-018-4265-x>
- Deng, M., E. Boopathi, J.A. Hypolite, T. Raabe, S. Chang, S. Zderic, A.J. Wein, and S. Chacko. 2013. Amino acid mutations in the caldesmon COOH-terminal functional domain increase force generation in bladder smooth muscle. *Am. J. Physiol. Renal Physiol.* 305:F1455–F1465. <https://doi.org/10.1152/ajprenal.00174.2013>
- Devine, C.E., and A.P. Somlyo. 1971. Thick filaments in vascular smooth muscle. *J. Cell Biol.* 49:636–649. <https://doi.org/10.1083/jcb.49.3.636>
- Driska, S.P., P.G. Stein, and R. Porter. 1989. Myosin dephosphorylation during rapid relaxation of hog carotid artery smooth muscle. *Am. J. Physiol.* 256: C315–C321. <https://doi.org/10.1152/ajpcell.1989.256.2.C315>
- Earley, J.J., X. Su, and R.S. Moreland. 1998. Caldesmon inhibits active crossbridges in unstimulated vascular smooth muscle: an antisense oligodeoxynucleotide approach. *Circ. Res.* 83:661–667. <https://doi.org/10.1161/01.RES.83.6.661>
- Fürst, D.O., R.A. Cross, J. De Mey, and J.V. Small. 1986. Caldesmon is an elongated, flexible molecule localized in the actomyosin domains of smooth muscle. *EMBO J.* 5:251–257. <https://doi.org/10.1002/j.1460-2075.1986.tb04206.x>
- Gu, Z., J. Kordowska, G.L. Williams, C.L. Wang, and C.M. Hai. 2007. Erk1/2 MAPK and caldesmon differentially regulate podosome dynamics in A7r5 vascular smooth muscle cells. *Exp. Cell Res.* 313:849–866. <https://doi.org/10.1016/j.yexcr.2006.12.005>
- Gunst, S.J., and W. Zhang. 2008. Actin cytoskeletal dynamics in smooth muscle: a new paradigm for the regulation of smooth muscle contraction. *Am. J. Physiol. Cell Physiol.* 295:C576–C587. <https://doi.org/10.1152/ajpcell.00253.2008>
- Guo, H., R. Huang, S. Semba, J. Kordowska, Y.H. Huh, Y. Khalina-Stackpole, K. Mabuchi, T. Kitazawa, and C.L. Wang. 2013. Ablation of smooth muscle caldesmon affects the relaxation kinetics of arterial muscle. *Pflugers Arch.* 465:283–294. <https://doi.org/10.1007/s00424-012-1178-8>
- Gusev, N.B. 2001. Some properties of caldesmon and calponin and the participation of these proteins in regulation of smooth muscle contraction and cytoskeleton formation. *Biochemistry (Mosc.)*. 66:1112–1121. <https://doi.org/10.1023/A:1012480829618>
- Hemric, M.E., and J.M. Chalovich. 1988. Effect of caldesmon on the ATPase activity and the binding of smooth and skeletal myosin subfragments to actin. *J. Biol. Chem.* 263:1878–1885. [https://doi.org/10.1016/S0021-9258\(19\)77959-9](https://doi.org/10.1016/S0021-9258(19)77959-9)
- Horiuchi, K.Y., and S. Chacko. 1989. Caldesmon inhibits the cooperative turning-on of the smooth muscle heavy meromyosin by tropomyosin-actin. *Biochemistry.* 28:9111–9116. <https://doi.org/10.1021/bi00449a023>

- Humphrey, M.B., H. Herrera-Sosa, G. Gonzalez, R. Lee, and J. Bryan. 1992. Cloning of cDNAs encoding human caldesmons. *Gene*. 112:197–204. [https://doi.org/10.1016/0378-1119\(92\)90376-Z](https://doi.org/10.1016/0378-1119(92)90376-Z)
- Ikebe, M., and S. Reardon. 1988. Binding of caldesmon to smooth muscle myosin. *J. Biol. Chem.* 263:3055–3058. [https://doi.org/10.1016/S0021-9258\(18\)69031-3](https://doi.org/10.1016/S0021-9258(18)69031-3)
- Jang, S.M., J.W. Kim, D. Kim, C.H. Kim, J.H. An, K.H. Choi, and S. Rhee. 2013. Sox4-mediated caldesmon expression facilitates differentiation of skeletal myoblasts. *J. Cell Sci.* 126:5178–5188. <https://doi.org/10.1242/jcs.131581>
- Janovick, J.A., K. Natarajan, F. Longo, and P.M. Conn. 1991. Caldesmon: a bifunctional (calmodulin and actin) binding protein which regulates stimulated gonadotropin release. *Endocrinology*. 129:68–74. <https://doi.org/10.1210/endo-129-1-68>
- Jiang, Q., R. Huang, S. Cai, and C.L. Wang. 2010. Caldesmon regulates the motility of vascular smooth muscle cells by modulating the actin cytoskeleton stability. *J. Biomed. Sci.* 17:6. <https://doi.org/10.1186/1423-0127-17-6>
- Katayama, E., G. Scott-Woo, and M. Ikebe. 1995. Effect of caldesmon on the assembly of smooth muscle myosin. *J. Biol. Chem.* 270:3919–3925. <https://doi.org/10.1074/jbc.270.8.3919>
- Katsuyama, H., C.L. Wang, and K.G. Morgan. 1992. Regulation of vascular smooth muscle tone by caldesmon. *J. Biol. Chem.* 267:14555–14558. [https://doi.org/10.1016/S0021-9258\(18\)42075-3](https://doi.org/10.1016/S0021-9258(18)42075-3)
- Khromov, A., A.V. Somlyo, D.R. Trentham, B. Zimmermann, and A.P. Somlyo. 1995. The role of MgADP in force maintenance by dephosphorylated cross-bridges in smooth muscle: a flash photolysis study. *Biophys. J.* 69:2611–2622. [https://doi.org/10.1016/S0006-3495\(95\)80132-3](https://doi.org/10.1016/S0006-3495(95)80132-3)
- Kilpatrick, L.M., A.N. Stephens, B.M. Hardman, L.A. Salamonsen, Y. Li, P.G. Stanton, and G. Nie. 2009. Proteomic identification of caldesmon as a physiological substrate of proprotein convertase 6 in human uterine decidual cells essential for pregnancy establishment. *J. Proteome Res.* 8:4983–4992. <https://doi.org/10.1021/pr900381a>
- Kudryashov, D.S., A.V. Vorotnikov, T.V. Dudnakova, O.V. Stepanova, T.J. Lukas, J.R. Sellers, D.M. Watterson, and V.P. Shirinsky. 2002. Smooth muscle myosin filament assembly under control of a kinase-related protein (KRP) and caldesmon. *J. Muscle Res. Cell Motil.* 23:341–351. <https://doi.org/10.1023/A:1022086228770>
- Kühn, H., A. Tewes, M. Gagelmann, K. Güth, A. Arner, and J.C. Rüegg. 1990. Temporal relationship between force, ATPase activity, and myosin phosphorylation during a contraction/relaxation cycle in a skinned smooth muscle. *Pflugers Arch.* 416:512–518. <https://doi.org/10.1007/BF00382683>
- Lash, J.A., J.R. Sellers, and D.R. Hathaway. 1986. The effects of caldesmon on smooth muscle heavy actinomyosin ATPase activity and binding of heavy meromyosin to actin. *J. Biol. Chem.* 261:16155–16160. [https://doi.org/10.1016/S0021-9258\(18\)66691-8](https://doi.org/10.1016/S0021-9258(18)66691-8)
- Li, A., R. Hardy, S. Stoner, J. Tuckermann, M. Seibel, and H. Zhou. 2013. Deletion of mesenchymal glucocorticoid receptor attenuates embryonic lung development and abdominal wall closure. *PLoS One*. 8:e63578. <https://doi.org/10.1371/journal.pone.0063578>
- Li, Y., M. Reznichenko, R.M. Tribe, P.E. Hess, M. Taggart, H. Kim, J.P. DeGnore, S. Gangopadhyay, and K.G. Morgan. 2009. Stretch activates human myometrium via ERK, caldesmon and focal adhesion signaling. *PLoS One*. 4:e7489. <https://doi.org/10.1371/journal.pone.0007489>
- Lin, J.J., Y. Li, R.D. Eppinga, Q. Wang, and J.P. Jin. 2009. Chapter 1: roles of caldesmon in cell motility and actin cytoskeleton remodeling. *Int. Rev. Cell Mol. Biol.* 274:1–68. [https://doi.org/10.1016/S1937-6448\(08\)02001-7](https://doi.org/10.1016/S1937-6448(08)02001-7)
- Liu, P., N.A. Jenkins, and N.G. Copeland. 2003. A highly efficient recombineering-based method for generating conditional knockout mutations. *Genome Res.* 13:476–484. <https://doi.org/10.1101/gr.749203>
- Lubomirov, L.T., S. Papadopoulos, S. Pütz, J. Welter, T. Klöckener, K. Weckmüller, M.A. Ardestani, D. Filipova, D. Metzler, H. Metzner, et al. 2017. Aging-related alterations in eNOS and nNOS responsiveness and smooth muscle reactivity of murine basilar arteries are modulated by apocynin and phosphorylation of myosin phosphatase targeting subunit-1. *J. Cereb. Blood Flow Metab.* 37:1014–1029. <https://doi.org/10.1177/0271678X16649402>
- Ma, X., and R.S. Adelstein. 2014. A point mutation in Myh10 causes major defects in heart development and body wall closure. *Circ. Cardiovasc. Genet.* 7:257–265. <https://doi.org/10.1161/CIRCGENETICS.113.000455>
- Malmqvist, U., A. Arner, R. Makuch, and R. Dabrowska. 1996. The effects of caldesmon extraction on mechanical properties of skinned smooth muscle fibre preparations. *Pflugers Arch.* 432:241–247. <https://doi.org/10.1007/s004240050130>
- Marston, S. 1988. Aorta caldesmon inhibits actin activation of thio-phosphorylated heavy meromyosin Mg²⁺-ATPase activity by slowing the rate of product release. *FEBS Lett.* 238:147–150. [https://doi.org/10.1016/0014-5793\(88\)80245-X](https://doi.org/10.1016/0014-5793(88)80245-X)
- Marston, S., D. Burton, O. Copeland, I. Fraser, Y. Gao, J. Hodgkinson, P. Huber, B. Levine, M. el-Mezgueldi, and G. Notarianni. 1998. Structural interactions between actin, tropomyosin, caldesmon and calcium binding protein and the regulation of smooth muscle thin filaments. *Acta Physiol. Scand.* 164:401–414. <https://doi.org/10.1111/j.1365-201X.1998.tb10696.x>
- Marston, S., K. Pinter, and P. Bennett. 1992. Caldesmon binds to smooth muscle myosin and myosin rod and crosslinks thick filaments to actin filaments. *J. Muscle Res. Cell Motil.* 13:206–218. <https://doi.org/10.1007/BF01874158>
- Marston, S.B., and W. Lehman. 1985. Caldesmon is a Ca²⁺-regulatory component of native smooth-muscle thin filaments. *Biochem. J.* 231:517–522. <https://doi.org/10.1042/bj2310517>
- Mauss, S., G. Koch, V.A. Kreye, and K. Aktories. 1989. Inhibition of the contraction of the isolated longitudinal muscle of the guinea-pig ileum by botulinum C2 toxin: evidence for a role of G/F-actin transition in smooth muscle contraction. *Naunyn Schmiedebergs Arch. Pharmacol.* 340:345–351. <https://doi.org/10.1007/BF00168521>
- Mayanagi, T., and K. Sobue. 2011. Diversification of caldesmon-linked actin cytoskeleton in cell motility. *Cell Adhes. Migr.* 5:150–159. <https://doi.org/10.4161/cam.5.2.14398>
- Morachevskaya, E.A., and A.V. Sudarikova. 2021. Actin dynamics as critical ion channel regulator: ENaC and Piezo in focus. *Am. J. Physiol. Cell Physiol.* 320:C696–C702. <https://doi.org/10.1152/ajpcell.00368.2020>
- Moreno-Domínguez, A., O. Colinas, A. El-Yazbi, E.J. Walsh, M.A. Hill, M.P. Walsh, and W.C. Cole. 2013. Ca²⁺ sensitization due to myosin light chain phosphatase inhibition and cytoskeletal reorganization in the myogenic response of skeletal muscle resistance arteries. *J. Physiol.* 591:1235–1250. <https://doi.org/10.1113/jphysiol.2012.243576>
- Morgan, K.G., and S.S. Gangopadhyay. 2001. Invited review: cross-bridge regulation by thin filament-associated proteins. *J Appl Physiol (1985)*. 91:953–962. <https://doi.org/10.1152/jappl.2001.91.2.953>
- Mulvany, M.J., and W. Halpern. 1977. Contractile properties of small arterial resistance vessels in spontaneously hypertensive and normotensive rats. *Circ. Res.* 41:19–26. <https://doi.org/10.1161/01.RES.41.1.19>
- Murphy, R.A., J.T. Herlihy, and J. Megerman. 1974. Force-generating capacity and contractile protein content of arterial smooth muscle. *J. Gen. Physiol.* 64:691–705. <https://doi.org/10.1085/jgp.64.6.691>
- Nerurkar, N.L., L. Mahadevan, and C.J. Tabin. 2017. BMP signaling controls buckling forces to modulate looping morphogenesis of the gut. *Proc. Natl. Acad. Sci. USA.* 114:2277–2282. <https://doi.org/10.1073/pnas.1700307114>
- Ngai, P.K., and M.P. Walsh. 1984. Inhibition of smooth muscle actin-activated myosin Mg²⁺-ATPase activity by caldesmon. *J. Biol. Chem.* 259:13656–13659. [https://doi.org/10.1016/S0021-9258\(18\)89793-9](https://doi.org/10.1016/S0021-9258(18)89793-9)
- Nichol, P.F., R.F. Corliss, J.D. Tyrrell, B. Graham, A. Reeder, and Y. Saijoh. 2011. Conditional mutation of fibroblast growth factor receptors 1 and 2 results in an omphalocele in mice associated with disruptions in ventral body wall muscle formation. *J. Pediatr. Surg.* 46:90–96. <https://doi.org/10.1016/j.jpedsurg.2010.09.066>
- Nichol, P.F., R.F. Corliss, S. Yamada, K. Shiota, and Y. Saijoh. 2012. Muscle patterning in mouse and human abdominal wall development and omphalocele specimens of humans. *Anat. Rec. (Hoboken)*. 295:2129–2140. <https://doi.org/10.1002/ar.22556>
- Paule, S.G., L.M. Airey, Y. Li, A.N. Stephens, and G. Nie. 2010. Proteomic approach identifies alterations in cytoskeletal remodelling proteins during decidualization of human endometrial stromal cells. *J. Proteome Res.* 9:5739–5747. <https://doi.org/10.1021/pr100525a>
- Pfitzer, G., and P.J. Boels. 1991. Differential skinning of smooth muscle: a new approach to excitation-contraction coupling. *Blood Vessels.* 28:262–267.
- Pfitzer, G., M. Schroeter, V. Hasse, J. Ma, K.H. Rösger, S. Rösger, and N. Smyth. 2005. Is myosin phosphorylation sufficient to regulate smooth muscle contraction? *Adv. Exp. Med. Biol.* 565:319–328, discussion:328:405–415. https://doi.org/10.1007/0-387-24990-7_24
- Pfitzer, G., C. Zeugner, M. Troschka, and J.M. Chalovich. 1993. Caldesmon and a 20-kDa actin-binding fragment of caldesmon inhibit tension development in skinned gizzard muscle fiber bundles. *Proc. Natl. Acad. Sci. USA.* 90:5904–5908. <https://doi.org/10.1073/pnas.90.13.5904>
- Puetz, S., M.M. Schroeter, H. Piechura, L. Reimann, M.S. Hunger, L.T. Lubomirov, D. Metzler, B. Warscheid, and G. Pfitzer. 2012. New insights into myosin phosphorylation during cyclic nucleotide-mediated smooth muscle relaxation. *J. Muscle Res. Cell Motil.* 33:471–483. <https://doi.org/10.1007/s10974-012-9306-9>

- Savin, T., N.A. Kurpios, A.E. Shyer, P. Florescu, H. Liang, L. Mahadevan, and C.J. Tabin. 2011. On the growth and form of the gut. *Nature*. 476:57–62. <https://doi.org/10.1038/nature10277>
- Schroeter, M.M., and J.M. Chalovich. 2005. Fesselin binds to actin and myosin and inhibits actin-activated ATPase activity. *J. Muscle Res. Cell Motil.* 26:183–189. <https://doi.org/10.1007/s10974-005-9009-6>
- Schubert, K.M., J. Qiu, S. Blodow, M. Wiedenmann, L.T. Lubomirov, G. Pfitzer, U. Pohl, and H. Schneider. 2017. The AMP-Related Kinase (AMPK) Induces Ca²⁺-Independent Dilatation of Resistance Arteries by Interfering With Actin Filament Formation. *Circ. Res.* 121:149–161. <https://doi.org/10.1161/CIRCRESAHA.116.309962>
- Shcherbakova, O.V., D.V. Serebryanaya, A.B. Postnikov, M.M. Schroeter, S. Zittrich, A.A. Noegel, V.P. Shirinsky, A.V. Vorotnikov, and G. Pfitzer. 2010. Kinase-related protein/telokin inhibits Ca²⁺-independent contraction in Triton-skinned guinea pig taenia coli. *Biochem. J.* 429: 291–302. <https://doi.org/10.1042/BJ20090819>
- Shimizu, Y., D. Thumkeo, J. Keel, T. Ishizaki, H. Oshima, M. Oshima, Y. Noda, F. Matsumura, M.M. Taketo, and S. Narumiya. 2005. ROCK-I regulates closure of the eyelids and ventral body wall by inducing assembly of actomyosin bundles. *J. Cell Biol.* 168:941–953. <https://doi.org/10.1083/jcb.200411179>
- Sobue, K., Y. Muramoto, M. Fujita, and S. Kakiuchi. 1981. Purification of a calmodulin-binding protein from chicken gizzard that interacts with F-actin. *Proc. Natl. Acad. Sci. USA.* 78:5652–5655. <https://doi.org/10.1073/pnas.78.9.5652>
- Somlyo, A.P., and A.V. Somlyo. 2003. Ca²⁺ sensitivity of smooth muscle and nonmuscle myosin II: modulated by G proteins, kinases, and myosin phosphatase. *Physiol. Rev.* 83:1325–1358. <https://doi.org/10.1152/physrev.00023.2003>
- Szpacenko, A., and R. Dabrowska. 1986. Functional domain of caldesmon. *FEBS Lett.* 202:182–186. [https://doi.org/10.1016/0014-5793\(86\)80683-4](https://doi.org/10.1016/0014-5793(86)80683-4)
- Totsukawa, G., E. Himi-Nakamura, S. Komatsu, K. Iwata, A. Tezuka, H. Sakai, K. Yazaki, and H. Hosoya. 1996. Mitosis-specific phosphorylation of smooth muscle regulatory light chain of myosin II at Ser-1 and/or -2 and Thr-9 in sea urchin egg extract. *Cell Struct. Funct.* 21:475–482. <https://doi.org/10.1247/csf.21.475>
- Van Eyk, J.E., D.K. Arrell, D.B. Foster, J.D. Strauss, T.Y. Heinonen, E. Furmaniak-Kazmierczak, G.P. Côté, and A.S. Mak. 1998. Different molecular mechanisms for Rho family GTPase-dependent, Ca²⁺-independent contraction of smooth muscle. *J. Biol. Chem.* 273:23433–23439. <https://doi.org/10.1074/jbc.273.36.23433>
- Velaz, L., R.H. Ingraham, and J.M. Chalovich. 1990. Dissociation of the effect of caldesmon on the ATPase activity and on the binding of smooth heavy meromyosin to actin by partial digestion of caldesmon. *J. Biol. Chem.* 265:2929–2934. [https://doi.org/10.1016/S0021-9258\(19\)39890-4](https://doi.org/10.1016/S0021-9258(19)39890-4)
- Wang, C.L. 2001. Caldesmon and smooth-muscle regulation. *Cell Biochem. Biophys.* 35:275–288. <https://doi.org/10.1385/CBB:35:3:275>
- Wang, C.L. 2008. Caldesmon and the regulation of cytoskeletal functions. *Adv. Exp. Med. Biol.* 644:250–272. https://doi.org/10.1007/978-0-387-85766-4_19
- Wirth, A., M. Schroeter, C. Kock-Hauser, E. Manser, J.M. Chalovich, P. De Lanerolle, and G. Pfitzer. 2003. Inhibition of contraction and myosin light chain phosphorylation in guinea-pig smooth muscle by p21-activated kinase 1. *J. Physiol.* 549:489–500. <https://doi.org/10.1113/jphysiol.2002.033167>
- Yamashiro, S., K. Yoshida, Y. Yamakita, and F. Matsumura. 1994. Caldesmon: possible functions in microfilament reorganization during mitosis and cell transformation. *Adv. Exp. Med. Biol.* 358:113–122. https://doi.org/10.1007/978-1-4615-2578-3_11
- Yamin, R., and K.G. Morgan. 2012. Deciphering actin cytoskeletal function in the contractile vascular smooth muscle cell. *J. Physiol.* 590:4145–4154. <https://doi.org/10.1113/jphysiol.2012.232306>
- Yuen, S.L., O. Ogut, and F.V. Brozovich. 2009. Nonmuscle myosin is regulated during smooth muscle contraction. *Am. J. Physiol. Heart Circ. Physiol.* 297:H191–H199. <https://doi.org/10.1152/ajpheart.00132.2009>
- Zhang, W., and S.J. Gunst. 2017. Non-muscle (NM) myosin heavy chain phosphorylation regulates the formation of NM myosin filaments, adhesion assembly and smooth muscle contraction. *J. Physiol.* 595: 4279–4300. <https://doi.org/10.1113/JP273906>
- Zheng, P.P., L.A. Severijnen, M. van der Weiden, R. Willemsen, and J.M. Kros. 2008. A crucial role of caldesmon in vascular development in vivo. *Cardiovasc. Res.* 81:362–369. <https://doi.org/10.1093/cvr/cvn294>

Supplemental material

Methods: EM

Urinary bladders from *Caldi^{+/+}* and *Caldi^{-/-}* fetuses, removed immediately after sacrifice from the animals at E18.5, were opened in the longitudinal direction and split in half as for mechanical experiments. The strips were mounted flat on small cork plates with pins; rapidly placed into 3% glutaraldehyde in 0.1 M cacodylate buffer, pH 7.2, for immersion fixation; and stored in this solution for 8 d at room temperature. After the pins and cork plate were removed, the tissues were trimmed in squares; rinsed 3× 30 min in 0.1 M cacodylate buffer, pH 7.2; postfixed for 4 h with 1% OsO₄ in 0.1 M cacodylate buffer, pH 7.2, at room temperature in the dark; rinsed again 4× 30 min in 0.1 M cacodylate buffer, pH 7.2; dehydrated at room temperature with ethanol (50% for 30 min; 70% overnight at 4°C; 90% for 30 min; and 100% for 3× 30 min) and propylenoxide (30 min, 1 part ethanol + 1 part propylenoxide; 2× 30 min, 100% propylenoxide); infiltrated with epon (5 h, 1 part propylenoxide + 1 part epon I without *N,N*-dimethylbenzylamine; overnight, 1 part propylenoxide + 3 parts epon I; 3× 3 h, epon I; 120 min, epon II containing *N,N*-dimethylbenzylamine); and embedded in epon II (polymerization for 48 h at 62°C). Ultrathin sections were cut at gray interference color (25–30 nm) with a 35° diamond knife (Diatome) on an Ultracut E (Leica), stretched with chloroform vapor, mounted on formvar/carbon-coated 200-mesh copper grids (5 μm bar thickness), and contrasted for 10 min with saturated (2%) uranyl acetate in 70% ethanol and for 5 min with 0.2% aqueous lead citrate, pH 11.8. Microscopy was performed on a Zeiss EM109 (80 kV; 500-μm condenser, 1 aperture; 200-μm condenser, 2 aperture; 30-μm objective aperture) equipped with a temperature-stabilized wide-angle YAC charge-coupled device camera at the side entry port (2,048 × 2,048 pixels, 12-bit grayscale/pixel). Magnification was calibrated with a cross grating replica (2,160 lines/mm, d = 0.463 μm). To enhance contrast, images were γ-adjusted.

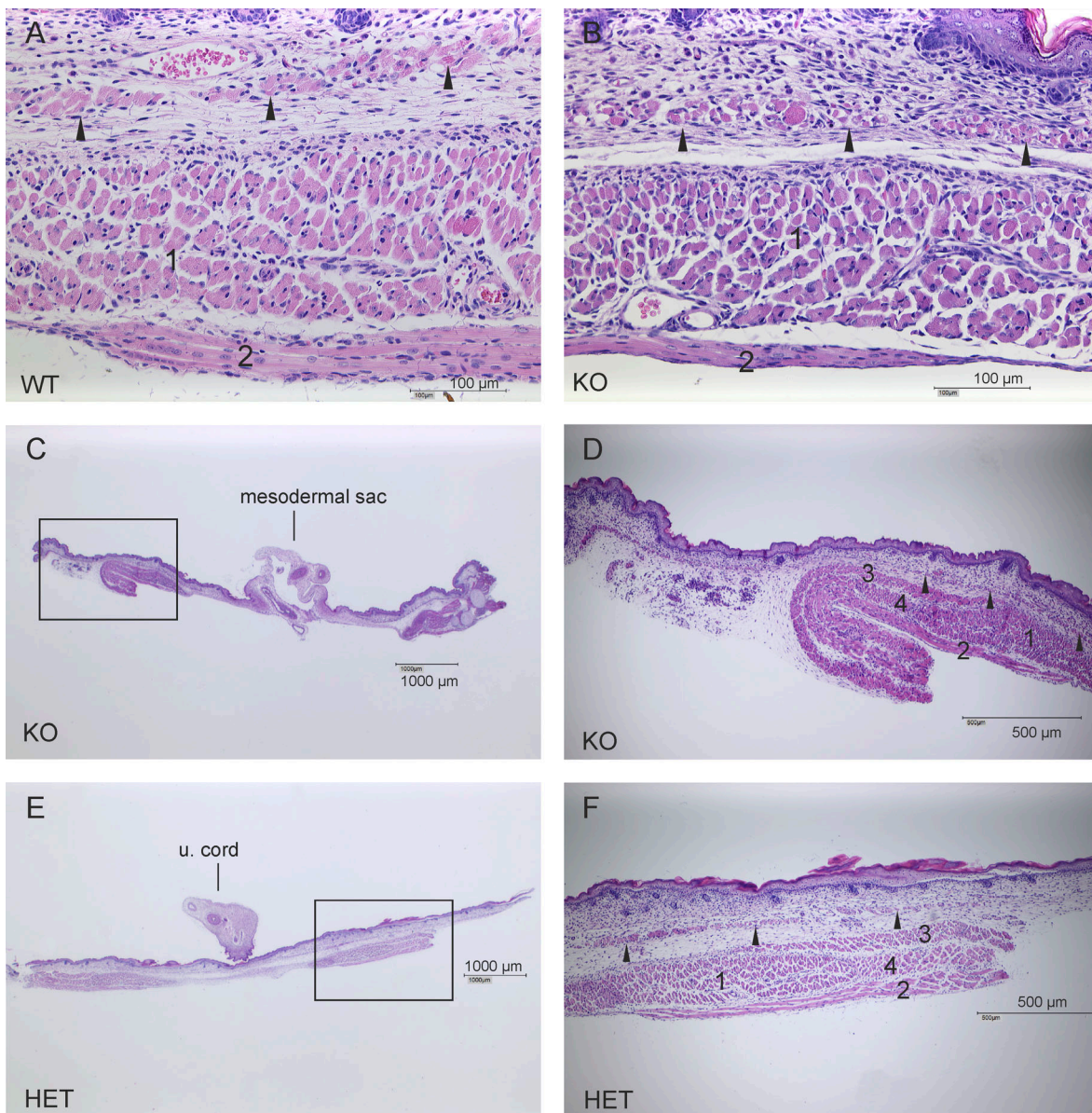


Figure S1. **Hematoxylin and eosin-stained sections of the ventral abdominal wall of E17.5 fetuses.** **(A and B)** Images of the same WT (A) and KO (B) fetuses shown in Fig. 4 at higher (20-fold) magnification depicting that the panniculus carnosus (arrowheads) was less well developed and discontinuous, and that the rectus (1) and transversus abdominis (2) were thinner and hypotrophic in KO. Myofibers could be discerned in the transversus abdominis. **(C and D)** Images of the ventral abdominal wall of another KO at 1.25-fold (C) and 5-fold (D) magnification, showing that the external (3) and internal (4) oblique muscles were present. The mesodermal sac that had contained the herniated gut was preserved in this fetus. We pushed the herniated gut gently into the abdominal cavity before dissecting the skin flap. **(E and F)** 1.25- and 5-fold magnification of a HET showing the umbilical cord and that all five muscles were well developed and the myofibers were oriented similar to WT. Representative images of two WT, four KO, and two HET fetuses.

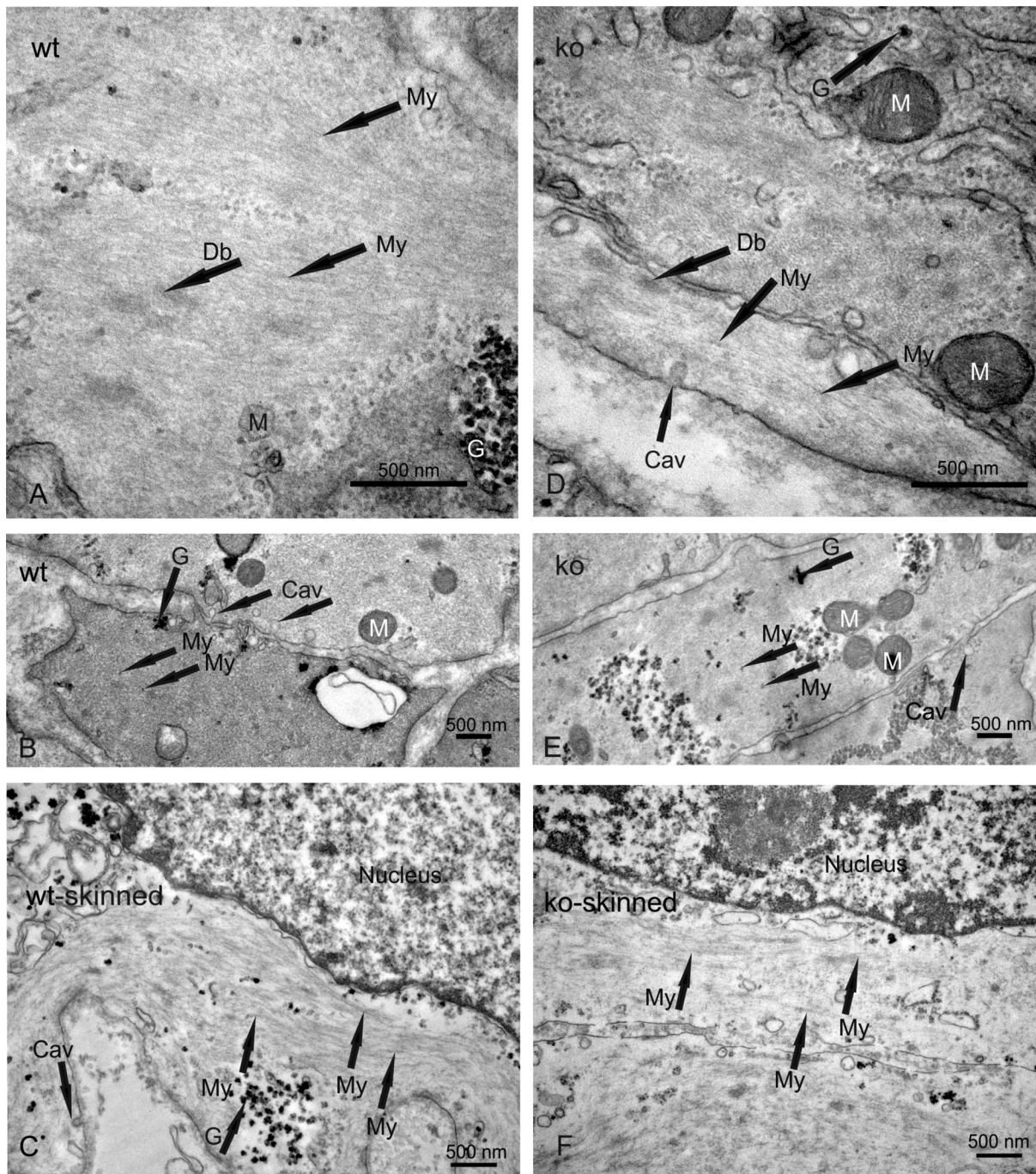


Figure S2. **Electron micrographs from E18.5 urinary bladder strips.** Upper panels: Longitudinal section. Middle panels: Cross section of intact bladder strips. Lower panels: Longitudinal section of skinned bladder strips. Images of smooth muscle cells showed glycogen particles (G), well developed mitochondria (M), and caveolae (Cav) alternating with dense bands along the plasma membrane in both intact *Cald1*^{+/+} and *Cald1*^{-/-} fetuses. Filaments were present in the cytoplasm, but the conservation of actin and myosin (My) filaments was not sufficient to discern differences between *Cald1*^{+/+} and *Cald1*^{-/-} bladder smooth muscle.